



HAL
open science

Kaolinite dating from Acrisol and Ferralsol: A new key to understanding the landscape evolution in NW Amazonia (Brazil)

Maximilien Mathian, Guilherme Taitson Bueno, Etienne Balan, Emmanuel Fritsch, Nádia Regina Do Nascimento, Madeleine Selo, Thierry Allard

► To cite this version:

Maximilien Mathian, Guilherme Taitson Bueno, Etienne Balan, Emmanuel Fritsch, Nádia Regina Do Nascimento, et al.. Kaolinite dating from Acrisol and Ferralsol: A new key to understanding the landscape evolution in NW Amazonia (Brazil). *Geoderma*, 2020, 370, pp.114354. 10.1016/j.geoderma.2020.114354 . hal-03047287

HAL Id: hal-03047287

<https://hal.science/hal-03047287>

Submitted on 14 Dec 2020

HAL is a multi-disciplinary open access archive for the deposit and dissemination of scientific research documents, whether they are published or not. The documents may come from teaching and research institutions in France or abroad, or from public or private research centers.

L'archive ouverte pluridisciplinaire **HAL**, est destinée au dépôt et à la diffusion de documents scientifiques de niveau recherche, publiés ou non, émanant des établissements d'enseignement et de recherche français ou étrangers, des laboratoires publics ou privés.

Kaolinite dating from Acrisol and Ferralsol: a new key to understanding the landscape evolution in NW Amazonia (Brazil)

Maximilien Mathian¹, Guilherme Taitson Bueno², Etienne Balan¹, Emmanuel Fritsch¹, Nádia Regina do Nascimento³, Madeleine Selo¹, Thierry Allard¹

¹Sorbonne Université, Institut de minéralogie, de physique des matériaux et de cosmochimie, UMR CNRS 7590, IRD, MNHN, Université Pierre et Marie Curie, 4 Place Jussieu, 75005, France

²Federal University of Goiás - UFG, Instituto de Estudos Socioambientais, Av. Esperança, s/n - Samambaia, Goiânia - GO, 74001-970, Brazil

³University of the State of São Paulo - UNESP Instituto de Geociências e Ciências Exatas, Rua 10, 2527, Rio Claro - SP, 13500-230, Brazil.

Abstract:

Ferralsols and Acrisols are major types of soils of the Amazon basin observed on various landform units comprising plateau surfaces, incised hills at their edges and slopes. The present study focuses on an Acrisol developed on plateau surfaces from northwest Amazonia and a Ferralsol from the convex hills of the incised plateau edges. Local geomorphologic models of weathering covers suggest that Ferralsols are younger than plateau Acrisols but the absolute chronology of their formation is still lacking. This type of information is however critical to understand the evolution of northwest Amazon Basin landscapes and to identify its link with major climatic and geomorphologic events. In this paper, kaolinite-rich samples from soils and saprolites belonging to a transect in the São Gabriel da Cachoeira region (Amazon state, Brasil) are investigated. Based on their crystal-chemical characters, several types of kaolinites are identified. Using a previously developed methodology based on electron paramagnetic resonance (EPR) spectroscopy, crystallization ages are proposed for these different kaolinites. Saprolite kaolinites are dated from 6 to 3.6 Ma in the Acrisol profile and display significantly more recent ages (< 1 Ma) in the Ferralsol saprolite. Kaolinite from *solum* (soils horizons above the C horizon) display ages ranging from 2.5 to 1 Ma for both the Acrisol and Ferralsol. Three distinct weathering stages are thus unraveled by kaolinite dating. The Acrisol saprolite displays the older weathering stage preserved in the investigated soil sequence. It is followed by a single weathering stage leading to the formation of both soils. These two stages can be correlated to the formation of two paleosurfaces recognized at the scale of the South America subcontinent as the Miocene Vehlas and the Quaternary Paraguaçu surfaces, indicating that the Curicuriari profiles evolved during periods favorable to tropical weathering surfaces development in Amazonia. The last weathering stage corresponds to the saprolite formation in the Ferralsol profile, which is still developing under the present Amazonian climate. This still active, late

38 weathering stage is tentatively related to the more significant drainage and relief dissection
39 occurring on the plateau edges.

40

41 **Keywords:** Laterite, EPR dating, Kaolinite, Ferralsol/Acrisol transition, Amazonia

42

43 **1. Introduction**

44

45 Tropical weathering covers extend over one third of the present-day continental surfaces
46 (Nahon, 2003) and develop over a large variety of climates, geological units and elevations.
47 They generally consist in indurated or unconsolidated regoliths with a mineralogy dominated
48 by various oxides/hydroxides/oxyhydroxides (iron, aluminium), kaolinite and quartz. During
49 the last 20 years, several methods have been developed to date secondary minerals (i.e. minerals
50 formed due to weathering), such as Ar/Ar dating of Mn oxides (Vasconcelos, 2015 and
51 reference therein), (U-Th)/He dating of iron oxides or oxyhydroxides (Shuster et al., 2005) and
52 electron paramagnetic resonance (EPR) dating of kaolinites (Balan et al., 2005). They
53 demonstrated that these minerals can be relics of intense weathering pulses that can be
54 associated to specific paleoclimatic conditions (Vasconcelos et al., 1999 and ref. therein; Balan
55 et al., 2005; Beauvais et al., 2008; Retallack et al., 2010; Bonnet et al., 2016; Allard et al.,
56 2018). However, a potential tectonic/eustatic control leading to water table falling and
57 impacting on the regolith development cannot be excluded, as suggested by Linton (1955),
58 Ollier (1988), Bland and Rolls (1998) and Taylor and Howard (1999). By deciphering past
59 preferential periods of weathering and documenting the expected links with these two classes
60 of processes, i.e., drainage and watertable migration, dating of secondary minerals improves
61 our understanding of regolith genesis and more generally of the evolution of continental
62 surfaces through geological time.

63

64 Among tropical weathering regions, the Amazon basin has been widely studied due to its
65 large size (about 7 millions km², Taitson Bueno et al., 2019), major input of water and
66 sediments to the oceans (Gaillardet, 1997) and diversity of regoliths (Richter and Babbar,
67 1991). The Brazilian project of natural resources mapping (Radam, 1972-1978) highlighted the
68 presence of four main types of soils in Amazonia: Ferralsols (rich in sesquioxides), Acrisols
69 (cations desaturated and displaying a clayey accumulation horizon at depth), groundwater
70 laterite/gleysols systems and giant waterlogged Podzols. Acrisols and Ferralsols are often
71 referred to as lateritic soils in the broad sense. We consider herein that the *solum* corresponds

72 to the horizons above the saprolite (C horizon) in a soil profile. In the upper Amazon basin,
73 transitions between Ferralsols, Acrisols and Podzols are observed (Radam, 1972-1978; Lucas
74 et al., 1987; Almeida et al., 2005; Fritsch et al., 2011). These soils are developed on various
75 primary rocks, from Amazonian sediments to granitoid rocks of the Guyana Shield or related
76 intrusions. An understanding of their genesis and interlink would be an important step in the
77 reconstruction of the evolution of the Amazon Basin landscape through space and time.

78

79 In the central Amazon Basin (Manaus region), Ferralsols developed at the expense of
80 sedimentary formation rich in kaolinite such as, e.g., the Alter do Chao formation (Lucas et al.,
81 1996; Montes et al., 2002; Balan et al., 2005). The kaolinites from these profiles are
82 increasingly disordered from bottom to top (Lucas et al., 1987; Balan et al., 2007). The dating
83 of these clay minerals leads to ages older than 25 Ma for the sedimentary horizons, indicating
84 extensive formation or transformation of kaolinite posterior to the late cretaceous deposition of
85 the sediments, and within 11 to 6 Ma for the soil horizons (Balan et al., 2005). These younger
86 Miocene ages were interpreted as reflecting kaolinite dissolution and recrystallization under the
87 action of supergene weathering fronts in the regolith.

88

89 The Ferralsol/Podzol (Lucas et al., 1996; Dubroeuq et Volkoff, 1998; Do Nascimento et
90 al., 2004; Ishida et al., 2014) or red to yellow Ferralsols transitions (Fritsch et al., 2005; Balan
91 et al., 2007) have been studied in the Amazon basin. The “yellowing process” of Ferralsols
92 proceeds with the progressive replacement of kaolinite, hematite and Al-poor goethite by Al-
93 rich goethite and gibbsite presumably resulting from the action of the present-day humid
94 climate (Fritsch et al., 2002; 2005). Yellowing of red Ferralsols, linked to mineralogical
95 transformations and changes in soil structure, was also described in other parts of the world,
96 such as Africa (Maignien, 1961; Chauvel et Pedro, 1978; Fritsch et al., 1989); it is mainly
97 related to the influence of climate and topography.

98

99 Acrisols and Ferralsols occupy a large part of the Amazonian landscape (Figure 1 A),
100 however the transition between them is still poorly understood. In large parts of the basin,
101 Acrisols occur mostly along the slopes of the incised plateaus, whereas the Ferralsols occur on
102 the well drained flat top surfaces of these plateaus. A related general model of evolution of
103 weathering covers through various stages of degradation as a function of topography and
104 involving successive processes such as hydromorphy and clay translocation was proposed (see
105 Melfi et al., 1996). This model describes a common sequence Ferralsols - Acrisols - Podzols

106 that is commonly encountered in the field through the Amazon basin. However, in the
107 northwestern part of the basin, where this study takes place, Ferralsols are specifically
108 developed on the plateaus incised edges, whereas Acrisols occur on the plateau centres
109 surrounding podzolized waterlogged areas. A comprehensive regional model of
110 geomorphological and pedological evolution was proposed by Taitson Bueno (2009) to account
111 for this particular distribution, where Acrisols are older than Ferralsols. However, no absolute
112 dating was yet performed to sustain this model and to understand the transition between the
113 involved weathering covers as a function of past orogenic or paleoclimatic forcing.

114

115 In the present study, one yellow Acrisol and one red Ferralsol profile, including their
116 respective saprolites, from one transect in the Sao Gabriel region (Rio Curicuriari watershed,
117 Brazil, NW Amazon Basin) were investigated. A special attention was paid to kaolinite dating
118 using the EPR dating methodology described in Balan et al. (2005). In unconsolidated tropical
119 soils, it is proposed that kaolinites form and recrystallize in large amount during intense
120 precipitation periods (Mathian et al., 2018) that can be related to known
121 paleoclimatic/geodynamic events. This study provides the chronology of the local development
122 of weathering profiles, investigates their potential relationship and then specifies the regional
123 model of geomorphological and pedological evolution.

124

125 **2. Location and description of soil profiles**

126

127 **2.1 Regional settings**

128

129 The study area is located in NW Amazonia (Brazil) on the K'Mudku Shear Belt formation
130 in the south of the Guyana shield (Santos et al., 2000). The present-day climate is described as
131 a monsoonal climate (i.e. with contrasting seasonal precipitations). The average temperature is
132 26.4°C, the mean annual air humidity set around 84% and the mean annual rainfalls are about
133 2900 mm per year.

134

135 The northern part of the Amazon basin displays transitions between three of the
136 characteristic soils of Amazonia: Ferralsols, Acrisols and seasonally waterlogged Podzols, as
137 reported in Fig. 1A (Radam, 1972-1978; Lucas et al., 1987; Almeida et al., 2005; Fritsch et al.,
138 2011, Taitson Bueno et al., 2019). The studied soil sequence is located in the Rio Curicuriari
139 area (Fig. 1), in the south of the Rio Negro basin near to the city of Sao Gabriel da Cachoeira
140 (northwest of Brazil). The topography of the region is fully described in Dubroeuq and Volkoff

141 (1988) and Allard et al. (2018). It consists in a succession of low elevation plateaus (about 80
142 m of altitude) incised by streams and rivers (Supporting Information (SI) 1). The regional
143 basement is dominated by mylonite rocks dated ca 1.20 Ga (Santos et al., 2000). However the
144 studied soils are developed on intrusive “Uaupés” granitoids, dated around 1.51 Ga and
145 preserved during the Shear Belt activation (Almeida, 2005). The Uaupés granitic enclaves are
146 mainly composed of monzogranite, a rock with a mineralogy dominated by feldspars, biotite,
147 titanite, amphibole, quartz, apatite and few accessory minerals as magnetite, ilmenite, and pyrite
148 (Dall’agnol and Macambira, 1992; Santos et al., 2000 and Almeida, 2005).

149
150 The western part of the Curicuriari basin is dominantly covered by Podzols, whereas the central
151 eastern part of this area is mainly covered by Ferralsols and Acrisols (Fig. 1B). Several
152 “pouches” of Podzols can be found in the dominant Acrisol zone of this region. Seldom, direct
153 contact between Ferralsols and Podzols can also be observed (Fig. 1B). At the regional scale,
154 the typical soil sequence on the flat plateau surface is Ferralsol-Acrisol-Podzol, from the plateau
155 edges to its center. The nature of soils is strongly linked to the topographical units in the
156 landscape. The Podzols formed over inundated plains and depressions, Acrisols on poorly
157 drained plateau surfaces and Ferralsols on the better drained dissected plateau edges. Similar
158 relations of soil types with the topography and hydrologic parameters have also been reported
159 in studies of other regoliths developed in Amazon region (Fritsch et al., 2011 and ref. therein).
160 In these previous studies, Podzols evolved at the expense of Acrisols and Acrisols at the
161 expense of Ferralsols, both transformations progressing from the center to the edges of plateaus
162 at a regional scale and upwards along the slopes at a local scale (Melfi et al., 1996). Indeed, the
163 dissection of plateau edges by stream incision enhanced drainage efficiency and eroded part of
164 the former plateau soils. On the flat or convex tops of residual hills the Ferralsols remained,
165 while along the new slopes a new generation of soils as Cambisols and Acrisols developed.

166
167 In contrast, the soil distribution in the Curicuriari region, with Ferralsol developed over incised
168 plateau edges and Acrisol on flat plateaus, raises questions about the lateral progression of
169 Ferralsols at the expense of the local Acrisols (Fig. 1C). On the other hand, Acrisols may result
170 from the complete transformation of older Ferralsols on the plateaus. Kaolinite dating in the
171 weathering covers should allow us to bring more decisive answers to these issues.

172

173 **3.2 Paleoclimates and geodynamic history of the Amazon basin**

174

175 The present-day climate of Amazon basin is a monsoonal system, driven by the Atlantic
176 moist air circulation and influenced by the Andean Cordillera (Vonhof and Kaandorp, 2010).
177 The Andean Cordillera blocks the present-day Atlantic easterlies to create a northwestern
178 barrier jet called the South-American low-level jet which is critical for the local and continental
179 climate establishment (Insel et al., 2009 and references). Precipitation is blocked on the east
180 side of the Andean Cordillera and thus a precipitation gradient is observed in Amazonia, from
181 the mountains chain to the Atlantic Ocean (Bookhagen and Strecker, 2008; 2010; Taitson
182 Bueno et al., 2019). Using climatic modelling, Insel et al. (2009) also explained that this
183 phenomenon blocked past dry westerlies originated from the Pacific Ocean, although no drastic
184 change of precipitation volume occurred over the Amazon basin due to Andean uplift.

185

186 Several studies addressed in detail the evolution of paleoclimate in the Amazon Basin.
187 Unlike other continental surfaces, Brazil has not substantially drifted northward since the
188 Mesozoic. This part of the world has experienced a relatively stable climate, mainly influenced
189 by global climatic variations. Tardy et al. (1991) proposed that a seasonally contrasted warm
190 and humid climate, favourable to tropical weathering surfaces formation (bauxites, iron
191 duricrusts, laterites), affected the Amazonia basin since the late Cretaceous (ca 70 Ma).

192

193 Global paleoclimatic fluctuations should have also affected the Amazon basin. The
194 evolution of ocean temperature is often used as a proxy for global temperature evolution,
195 including continental temperatures. Warmer temperatures can also be linked to higher
196 precipitations on the continent due to a strengthening of oceanic evaporation. Accordingly,
197 warm periods can coincide with peaks of precipitations and temperature in Amazonia. Five
198 main temperature peaks (SI 2) during the Tertiary were reported by Zachos et al. (2001) and
199 confirmed by Cramer et al. (2009): the Palaeocene/Eocene Temperature Maximum (PETM),
200 Early Eocene Climatic Optimum (EECO), Mid-Eocene Climatic Optimum (MECO), Late
201 Oligocene Warming (LOW) and Mid-Miocene Climatic Optimum (MMCO). Present day
202 variations of rainfall intensity between summer and winter are inherited from the migration of
203 the intertropical convergence zone (ITCZ) between the two seasons. Accordingly, factors that
204 influence the ITCZ location, e.g. Milankovitch cycles, also influence the Amazonian climate
205 (Vonhof et Kaandrop, 2010). Accordingly, several authors described an increase of rainfall in
206 South America between 5 and 4 Ma, linked to ITCZ variations (Hovan, 1995 and Billups et al.,
207 1999).

208

209 In addition to the global climatic changes, two major geodynamic events have influenced
210 the Amazon basin climate during the Tertiary (SI 2): the Andean uplift phases (Bookhagen and
211 Strecker, 2008; 2010; Sepulchre et al., 2010) and the closure of the Panama seaway (Sepulchre
212 et al., 2010; Karas et al., 2017). Several uplifts phases have been reported for the Andean
213 orogeny (Hoorn et al., 2010; Campbell et al., 2006, and ref. therein). It begun in the Early
214 Jurassic with an independent development of the northern and central part of the cordillera,
215 which joined during the Miocene. Before that, Pacific westerlies and Atlantic easterlies joined
216 over the Amazon basin, causing more homogeneous precipitations (Sepulchre et al., 2010). The
217 present-day rainfalls gradient was established with the Quechua I uplift phase between 17-15
218 Ma and their forcing on air circulation. Accordingly, the Amazonian monsoonal system exists
219 since at least 15 Ma (Vonhof et Kaandrop, 2010 and ref. therein). Three others uplifts events in
220 the last 10 Ma are also reported: the Quechua II uplift (9.5-8.5 Ma) following the Ucayali
221 peneplains event, the Quechua III (ca 6 Ma) uplift and the last Pliocene uplift event (ca 4 Ma).
222 Due to their influence on the air mass circulation (Insel et al., 2009), these events potentially
223 caused variations in the local monsoon intensity.

224

225 The final closure of the Panama seaway at ca 3.5 Ma (or earlier, see Montes et al., 2015)
226 also influenced the Amazonian climate, affecting the oceanic circulation and Atlantic salinity
227 and temperature. During the Pliocene and Quaternary, the Amazonian climate remained
228 tropical but became drier and colder after the Panama closure according to Rosetti et al. (2005)
229 and ref. therein.

230

231

232 **2.3 Description of soil transect and profiles**

233

234 The Caju-Cobra transect (Fig. 1B, Fig. 2, SI 1) of about 1.6 km long is located in the
235 south of the Curicuriari river (Fig. 2). It is characterized by the presence of the two main soil
236 transitions of the Curicuriari catchment: 1) the lateral transition between the dominant Ferralsol,
237 located along the Rio Curicuriari river, and Acrisol; 2) the lateral transition between Acrisol
238 and waterlogged Podzol. While the second is characterized by a clear limit between the two
239 types of soils, the limit between Ferralsol and Acrisol is less well defined, as it mainly consists
240 in subtle changes in iron oxide nature and clay mineral content.

241

242 Two regolith profiles, including soils and saptrolites, have been selected from the Caju-

243 Cobra transect: one representative of Ferralsol, the Caju profile (CA), and one representative
244 of Acrisol, the Cobra profile (CO2). Both profiles are poorly differentiated, with only six thick
245 horizons detected. These horizons are described in the Table 1.

246

247 Both CA and CO2 profiles display A (organic rich), B (rich in kaolinites and iron
248 oxides/oxy-hydroxides; soil structure) and BC/C (soil/saprolite transition) horizons with
249 different colors. According to observations in the field, the Acrisol exhibits a slight clay
250 depletion in surficial horizons. The major horizons have similar thickness in the two profiles,
251 as the A, B and saprolite begin and stop at almost the same depth. In both profiles, the saprolite
252 is 2m deep (Table 1). For the present study, twelve samples were collected at similar depths
253 from the CA and CO2 profiles (Fig. 2). Note that the primary rocks have not been reached using
254 the auger for both profiles but eroded blocks of a monzogranite were collected in the rivers
255 surrounding the transect.

256

257

258 **3. Material and Methods**

259

260 All collected samples were sieved at 2 mm and dried at room temperature. The kaolinite-
261 enriched fractions were obtained after three steps: 1) The removal of residual organic matter
262 using H₂O₂; 2) The dissolution of iron oxides/oxyhydroxides using Citrate-Dithionite-
263 Bicarbonate treatments (Mehra and Jackson, 1960); 3) The collection of the inferior to 2 μm
264 grain size fractions of the samples using sedimentation. Magnetic oxides of the Ferralsol
265 samples that would hinder EPR measurement were removed by stirring their infra 2μm
266 fractions in water with a magnet for 24 hours.

267

268 X-ray diffraction (XRD) measurements were performed on powders of the bulk < 2mm
269 fraction of the samples with a Panalytical Pro MPD equipped with a X'Celerator detector and
270 Co-K α radiations. XRD patterns were recorded with a 2 θ range of 3 to 65°, with steps of 0.017°
271 and an acquisition time of 480 ms/per step.

272

273 Chemical analyses were performed at the Service d'Analyse des Roches et Minéraux
274 (SARM, Nancy, France) by inductively coupled plasma atomic optical emission spectrometry
275 (ICP-OES) for major elements quantification and inductively coupled plasma atomic mass

276 spectrometry (ICPMS) for the trace elements quantification. The complete procedure and
277 experimental errors are described at <http://www.cprg.cnrs-nancy.fr/SARM/index.html>.

278

279 Uranium mapping in raw samples was performed using ^{235}U induced fission tracks on
280 polished thin sections obtained from resin embedded samples (see part 3.2). Kapton® foils
281 covering the thin sections were used as external detectors (see Price and Walker, 1963 and
282 Kleeman and Lovering, 1967). The samples and standard glasses (SRM- 613 from the National
283 Bureau of Standard, Washington) were irradiated using thermal neutrons at the FRM2 reactor
284 in Munich (Germany). An instant flux of $1.15 \cdot 10^{13}$ n/cm²/s was used during 600s. The
285 revelation of fission tracks, recorded inside the Kapton® foils, was performed by an etching of
286 8 minutes in an aqueous solution of 14% NaClO and 12% NaCl heated at 100 °C (Sélo, 1983).
287 Fission tracks were counted using an optical microscope with an objective of 10x100
288 magnification in transmitted light.

289

290 Kaolinite crystal-chemistry was investigated using Fourier transform mid-infrared
291 spectroscopy (FTIR) and Electron Paramagnetic Resonance spectroscopy (EPR). Transmission
292 FTIR spectra were acquired using solid pellets, made of 1 mg of <2 μm samples and 150 mg
293 of KBr, using a Nicolet Magna 560 FTIR spectrometer. Each spectrum had a resolution of 2
294 cm⁻¹ in the 400-4000 cm⁻¹ range and was obtained by averaging 100 scans.

295

296 EPR spectra were obtained using a Bruker EMXplus™ spectrometer equipped with a high
297 sensibility cavity at X-Band (9.86 GHz). Acquisitions have been performed with a microwave
298 power of 40 mW, a magnetic field modulation with frequency of 100 kHz and amplitudes from
299 0.3 mT (Radiation Induced Defects (RID) spectra) to 0.5 mT (total spectra). The EPR signals
300 are characterized by effective g values defined by the resonance condition:

301

$$302 \quad h\nu = g\beta H \quad (1)$$

303

304 where h is the Planck constant, ν the hyperfrequency, β the Bohr magneton and H the magnetic
305 field. The DPPH standard (g = 2.0036) was used to calibrate the g values. The powders of infra
306 2μm samples were measured by this spectrometer in suprasil grade silica tubes at room
307 temperature. To compare the intensity of each EPR spectra, the spectra were normalized using
308 their height in the tubes, their weight and their recording gain. Reproducibility tests, focused

309 on the variation of the spectrometer gain and the samples weight and height, point to a 2σ
310 standard error equal to 10% on the measured RID normalized amplitude.

311

312 Dosimetry curves were obtained using artificial irradiations performed on the ARAMIS
313 electrostatic accelerator (Orsay, France). A beam of 1.5 MeV He^+ ions with a 0.3 A current was
314 used to simulate radiation effects due to alpha particles on kaolinite structure for six different
315 fluences ($3 \cdot 10^{11}$, $6 \cdot 10^{11}$, 10^{12} , $3 \cdot 10^{12}$, $6 \cdot 10^{12}$ and 10^{13} ions. cm^{-2}). The amount of irradiated sample
316 for each fluence was 30 mg (see 3.2 part), which was deposited on circulate steel plate to obtain
317 a thickness of 4 μm corresponding to the range of 1.5 MeV He^+ ions in kaolinite. After
318 irradiation, the unstable defects formed inside the kaolinite structure where annealed by 2 hours
319 heating at 250°C (Allard et al., 1994). The A-center content is assessed from the amplitude of
320 the signals of natural or irradiated and annealed samples.

321

322

323 **4. Ferralsol and Acrisol samples characterization**

324 **4.1 Mineralogy from XRD and FTIR spectroscopy**

325 The bulk mineralogy of the Ferralsol regolith (CA) is dominated by quartz and gibbsite.
326 In this case, gibbsite appears to be the main product formed in the first stages of the
327 monzogranite weathering (Fig 3B), as also observed in other sites of the Amazon basin
328 (Dubroeuq and Volkoff, 1988; Lucas et al., 1996; Furian et al., 2001). This observation is also
329 consistent with the observation of Shvartsev (2012) which defended that gibbsite is one of the
330 first phases developed during the weathering of Al-rich rocks. In this case, gibbsite precipitation
331 can promote the kaolinite crystallization from the remaining weathering fluids. Other studies
332 confirm this observation, some authors demonstrated the formation of gibbsite during the early
333 stage of granite and gneiss weathering in soils with a high drainage (Herrmann et al., 2007)
334 when other observed that gibbsite is one of the first secondary mineral formed at the expanse
335 of feldspars in the well-drained parts of lateritic saprolites (Anand et al., 1985). In the Ferralsol
336 profile, kaolinite and hematite are also present in all the samples, excepted CA 480. The reddish
337 coloration of these regolith horizons is consistent with the detection of hematite by XRD (Fig.
338 3B) that can also be linked to the important Fe concentration of the samples (ranging between
339 4 to 11%, see SI 3A). The presence of hematite indicates a relatively low water activity and a
340 good soil aeration, which is consistent with the free drainage conditions of this profile. A

341 noticeable increase of the kaolinite relative content (SI 5) is observed from the saprolite to the
342 soil samples (Fig. 3B), which coincides with a relative decrease in the gibbsite content. With
343 its progressive dissolution from bottom to top, gibbsite acts as an aluminium source
344 participating to kaolinite formation, also supplied by silica released from partial dissolution of
345 quartz and biogeochemical recycling of silica in the topsoil (Lucas et al., 1996). These
346 observations are consistent with the chemical trend (SI 3 and 4), in which the Al/Zr ratio
347 decreases from bottom to top and Si/Zr decreases in the profile base but accumulates in the
348 topsoil. The comparison between the evolution of quartz and gibbsite proportion along this
349 profile indicates the relative quartz content increases from saprolite to soil (SI 5). The gibbsite
350 replacement by kaolinite should be faster than the quartz dissolution. The peculiar mineralogy
351 of CA 480 sample may correspond to that of a lower weathering grade of primary rocks.
352 Presence of kaolinite and gibbsite in the clay fraction ($< 2 \mu\text{m}$) is confirmed by the FTIR spectra
353 (Fig. 4 D). In all the samples, characteristic OH stretching bands ascribed to kaolinite and
354 gibbsite are observed (Farmer 1974; Balan et al. 2001; Balan et al. 2006). It is worthy to note
355 that the mineralogical evolution in the Ferralsol profile is different from that related to the
356 yellowing process affecting the Ferralsol (i.e kaolinite, hematite and Al-poor goethite
357 replacement by Al-rich goethite and gibbsite) in the Manaus area as described by Fritsch et al.
358 (2005). The well-drained Ferralsol *solum* horizons seem more favourable to the kaolinite
359 precipitation than to the goethite and gibbsite formation, despite that the Amazonian climate
360 has been described as favourable to both minerals formation (Fritsch et al., 2011).

361

362 The bulk mineralogy of the Acrisol (CO2) profile (Fig. 3A) is different from that of the
363 Ferralsol one. Quartz and kaolinite are the major minerals. The yellow coloration dominantly
364 arises from goethite (Schwertmann, 1993). Goethite is detected as two broad XRD peaks at
365 4.19 \AA and 2.70 \AA , corresponding to the d(101), overlapping with the d(-1-11) peak of the
366 kaolinite, and the d(301) reflections, respectively. The low intensity of goethite peak attest to
367 its low content consistent with the low Fe concentration of the samples (ranging between 0.9 to
368 4 %, see SI 3B). The presence of goethite indicates a relatively high-water activity and is
369 consistent with the poor drainage conditions expected for the plateau Acrisol. Its proportion
370 seems to decrease in favor of a low hematite content in the 3 top samples of this acrisol profile.
371 Gibbsite is present in the *solum*, (from CO2 280 to 25), but its content decreases in the topsoil
372 samples (SI 5). The kaolinite/quartz ratio decreases from the saprolite samples to the topsoil.
373 Within the Acrisol *solum*, the CO2 200 sample displays the highest relative contribution of
374 kaolinite compared to quartz (SI 5). It corresponds to the clay accumulation horizon

375 characteristic from Acrisols. As for the Ferralsol, the transition between saprolite and Acrisol
376 *solum* is well marked. It is characterized by a significant decrease of kaolinite content from the
377 former to the latter. Anatase (TiO₂) is also present in the samples. The FTIR spectra of the clay
378 fractions (Fig. 4C) indicate that kaolinite is the main phase in this fraction, whereas gibbsite,
379 detected from CO₂ 280 to the top profile, remains a minor phase.

380
381 Additional information about the crystal-chemistry of kaolinite can be inferred from the
382 OH stretching bands (Farmer, 1974; Russel and Fraser, 1994; Balan et al., 2007; 2010). The
383 bands observed at 3698, 3670, 3650 and 3620 cm⁻¹ and a high 3670/3650 cm⁻¹ intensity ratio
384 characterize well-ordered kaolinites. In addition, the progressive broadening of the 3670 and
385 3650 cm⁻¹ bands expresses the increase of stacking disorder of kaolinite. The IR spectra of the
386 Ferralsol profile samples (CA, Fig. 4D) are characteristic of disordered kaolinites with a slight
387 order increase toward the top of the profile (except the deepest sample CA 485 which is
388 relatively similar to the CA 240 one). FTIR spectra of Acrisol profile (CO₂) kaolinites
389 correspond to well-ordered kaolinites.

390
391 The infrared spectra of kaolinite also display a weak signal at 3600 cm⁻¹ which is ascribed
392 to OH groups bound to Fe²⁺ ions. It attests for minor substitution of Fe³⁺ for Al³⁺ in the kaolinite
393 structure. The signal is more intense in samples of the Acrisol (CO₂) profile and increases from
394 saprolite to *solum*. In the Ferralsol (CA) profile, the signal is very weak and only observed in
395 the most surficial soil samples.

396
397 In both profiles, the FTIR signal of kaolinite and gibbsite allows one to clearly distinguish
398 the soils from the corresponding saprolites. In addition, they also demonstrate that the kaolinites
399 from the two profiles have specific crystal-chemical characters such as crystalline disorder and
400 structural iron, indicating that they formed under different conditions. Consequently, these data
401 suggest that the horizons in the Acrisol profile, including the saprolite, cannot be considered as
402 relictual material arising from an ancient Ferralsol. All the analyzed soils and saprolites are
403 distinct units.

404

405 **4.2 Electron paramagnetic resonance spectra of clay fractions**

406

407 EPR spectroscopy is a sensitive technique enabling the detection of species with unpaired
408 electrons, such as some cations of transition elements or electronic defects (Calas et al., 1988).
409 The EPR spectra of the < 2 μm fractions are characteristic of kaolinite (Fig. 4). Two types of

410 signal in the $g=4$ zone can be attributed to structural Fe^{3+} in kaolinite: the $Fe^{3+}_{(II)}$ signal, with
411 bands at $g \sim 4.17$ and 3.69 is ascribed to well-ordered domains whereas the $Fe^{3+}_{(I)}$ signal,
412 corresponding to a band near $g = 4.19$, is related to disordered structures such as the one
413 resulting from stacking faults (Gaite et al., 1997; Balan et al., 1999; 2000; 2007). Accordingly,
414 disordered kaolinite is characterized by a relatively intense $Fe^{3+}_{(I)}$ signal, while a well-ordered
415 one is defined by a dominant $Fe^{3+}_{(II)}$ signal. The EPR observations are consistent with FTIR
416 spectroscopy data, the well-ordered kaolinites from the Acrisol profile (CO2) displaying a
417 larger relative contribution of the $Fe^{3+}_{(II)}$ signal than those from the Ferralsol profile (CA). EPR
418 thus confirms that these profiles contain different types of kaolinites, formed under different
419 geochemical conditions. Based on the EPR signal of structural iron as a probe of structural
420 order, four main types of kaolinite can be distinguished within Ferralsol profile samples. They
421 are referred to as CA1, CA2, CA3 and CA 4, with the CA 4 the most disordered and CA 2 the
422 less disordered type (Table 2). Similarly, four types of kaolinite referred to as C1, C2, C3 and
423 C4, with C4 the less disordered and C2 the most disordered type, can be distinguished in the
424 Acrisol profile (CO2) (Table 3). The corresponding variations of crystalline order are however
425 moderate: 1) kaolinites from the Ferralsol saprolite are slightly more disordered than the one of
426 the soil samples; 2) kaolinites from the Acrisol saprolite are slightly more ordered than the one
427 of the soil samples. These 4 types of kaolinites disorder is the clue that these kaolinites likely
428 formed in different geochemical environment (e.g. Mathian et al., 2019). The Ferralsol (CA)
429 and Acrisols (CO2) profiles do not display a progressive evolution from well-ordered kaolinite
430 at the bottom to strongly disordered one in top soil horizon, as observed in the Manaus region
431 (Lucas et al., 1987; Balan et al., 2007). However, in these profiles, a mixing of kaolinites with
432 different crystalline orders cannot be excluded. In both regoliths, the transition between the soil
433 horizon and the saprolite observed at a macroscopic scale also corresponds to a boundary in
434 terms of kaolinite ordering.

435
436 In the $g=2$ region (Fig. 5), a signal related to trace content of vanadyle VO^{2+} ($S=1/2$)
437 molecular ions is also observed. This spectrum has been previously observed in kaolinite and
438 dickite (a kaolinite-group mineral with different stacking order) samples from sedimentary
439 (Muller & Calas, 1993) or hydrothermal (Mosser et al., 1996) origin. The same spectrum is
440 observed in kaolinite and dickite, exhibiting a hyperfine structure with 8 components (Hall et
441 al., 1980; Gehring et al., 1993).

442
443 The vanadyle spectrum is superimposed to the spectrum related to radiation-induced

444 defects (RID) which also occurs in the $g=2$ region. Various RIDs can be formed within the
445 kaolinite structure (Clozel et al., 1994 ; Allard et al., 2012). In the investigated samples, this
446 spectrum mainly corresponds to that of the A-center with signals at $g = 2.049$ ($g //$), and $g =$
447 2.006 ($g \perp$) (Fig. 5). This center consists in an electron hole located on an oxygen atom (Angel
448 et Jones, 1964; Clozel et al., 1994), produced by natural ionizing radiation (α , β and
449 γ radiations).

450
451

452 **5. Calculation of kaolinite ages**

453

454 Because of their thermal stability, A-centers accumulate in the kaolinite structure since
455 its crystallization and can be used as a geochronometer consistent with geological time scales
456 (Balan et al., 2005; Allard et al., 2018; Mathian et al., 2018). The kaolinite dating involves three
457 steps: (i) measurement of the EPR signal intensity of A-center in the collected sample, (ii)
458 determination of the natural radiation dose that affected these kaolinites since their
459 crystallisation (the so-called paléodose), (iii) interpretation of the paleodose in the light of the
460 natural radiation dose rate, enabling the determination of kaolinite age. Step (ii) requires the
461 determination of the relation between the signal intensity of A-centers and the radiation dose
462 using artificial irradiation experiments.

463
464

465 **5.1 Intensity of A-center signal**

466

467 The intensity of the $g \perp$ component is used to estimate the variations of A-center concentration
468 in kaolinite sample. As it interferes with the most intense resonance of the vanadyle spectrum
469 (Fig. 5), vanadyle contribution has been corrected by a linear extrapolation using the VO^{2+} band
470 located at $g = 1.881$ (only attributed to VO^{2+}) and a reference spectrum with dominant VO^{2+}
471 signal (dimex dickite; Balan et al. 1999; Premovic et al., 2011), as expressed in equations 2 and
472 3.

473

$$474 \quad R_{VO^{2+}} = \frac{I_{zs}}{I_{zdim}} \quad (2)$$

475 where I_{zdim} is the normalised intensity of the signal at $g = 1.881$ of the EPR spectrum of dimex
476 sample and I_{zs} : the normalised intensity of the same signal in the EPR spectrum of the studied
477 sample (Figure 5 A, B).

478

$$479 \quad I_{RID} = TI_s - TI_{dim} \times R_{VO}^{2+} \quad (3)$$

480

481 Where I_{RID} is the EPR signal intensity of A-centers, TI_s is the normalized intensity of the
482 EPR signal at $g = 2.006$ of the studied sample and TI_{dim} is the normalized intensity of the signal
483 at $g = 2.006$ of the dimex sample (Fig. 5 A, B).

484

485 The initial $g=2.006$ intensity and the obtained RID intensities (I_{RID}) are both presented in the SI
486 6. The resulting calculated intensities related to A-center range between 0.24 to 5.58 arbitrary
487 units (A.U.) for the Ferralsol CA, and 0 to 21.23 A.U. for the Acrisol CO2.

488

489 **5.2 Paleodose determination**

490

491 Four samples from the Ferralsol profile (CA 84, CA 200, CA 440, CA 480) and four from
492 the Acrisol profile (CO2 45, CO2 200, CO2 280, CO2 450) have been selected for artificial
493 irradiation (Table 1). The resulting dosimetry curves have been fitted using an exponential
494 function (Allard et al., 1994) combined with a linear parameter (F1), as described in Duval
495 (2012) and Allard et al. (2018), to enhance the fit precision:

496

$$497 \quad I = I_{\infty} \times (1 - e^{-\mu(D+P)}) + F1 \times (D + P) \quad (4)$$

498

499 where I is the RID concentration, I_{∞} is the RID concentration at saturation, μ is an efficiency
500 factor, P is the natural paleodose, D is the artificial dose rate and $F1$ is a linear factor.

501

502 The fitting parameters of dosimetry curves are presented in the SI 7. The paleodoses
503 (Tables 2 and 3) range from $1.21_{+/-0.24}$ kGy to $27.59_{+/-8.81}$ kGy for the Ferralsol CA (Fig. 6A), and
504 $23.92_{+/-6.54}$ to $100.92_{+/-27.32}$ kGy for the Acrisol CO2 (Fig. 6B). The errors on the paleodose have
505 been calculated using a Monte Carlo simulation based on an experimental error of 15% on each
506 point of the curve data set as described in Mathian et al. (2018).

507

508 Paleodose estimation for non-irradiated samples were performed using the approach of
509 Balan et al. (2005) and Mathian et al. (2018). It is based on the assumption that kaolinites with
510 a similar disorder will accumulate radiation-induced defects according to a same dosimetry
511 function (Allard et al., 1994). The fitting parameters of the dosimetry curve from the irradiated

512 kaolinite were extrapolated to the ones with a similar disorder, providing an estimate of
513 paleodose. The group of extrapolations are detailed in the Tables 2 and 3: the CA 84, CA 200,
514 CA 440, CA 480 fitting parameters have been used, for CA1, CA2, CA3 and CA4-types
515 kaolinites, respectively. Concerning CO₂, the parameters of CO₂ 45, CO₂ 200, CO₂ 280 and
516 CO₂ 450 have been used for the C1 C2, C3 and C4-types kaolinites, respectively.

517

518 Note that differences in the kaolinite/gibbsite ratio between samples of the same disorder
519 family cause a slight underestimation of the paleodose for samples containing more gibbsite
520 than their irradiated reference (as for CO₂ 55) and overestimation for the reverse case (as for
521 CA 240 and 280 samples). Beside this incertitude, the extrapolation methodology also induces
522 an additional error on the estimated paleodose (Mathian et al., 2018), which is added to the
523 errors related to the determination of initial dosimetry curves. Accordingly, ages determined on
524 extrapolated samples are less accurate than those obtained on irradiated samples.

525

526 **5.3 Dose rate determination**

527

528 The dose rate of each sample was calculated using the formula from Aitken (1985) and
529 the concentrations from U, Th and K (Table 2 and 3). Note that due to the small amount of
530 sample, the bulk chemistry of CO₂ 405, CA 485 and 380 samples has not been analyzed and
531 no age can be given for these samples.

532

533 The dose rate of the cosmic rays is small and decreases exponentially within the first soil
534 meter (Aitken, 1985), and was neglected for these calculations. The resulting uncorrected dose
535 rate range from 29.18_{+/-2.1} to 70.87_{+/-3.55} Gy/ka for the Ferralsol profile (CA) samples and from
536 19.62_{+/-1.44} to 46.93_{+/-2.92} Gy/ka for the Acrisol profile (CO₂) (Table 2 and 3).

537

538 However, the dose rate inferred from chemical composition is a raw value and does not
539 directly correspond to efficient natural irradiation of kaolinites because of three main factors:
540 1) the role of the spatial distribution of radioelements in the external irradiation of kaolinite; 2)
541 potential radon escape; 3) attenuation effects related to the water content of the soil samples.
542 These three factors can decrease the dose rate actually experienced by kaolinites with respect
543 to that inferred from chemical compositions only. Corresponding corrections of raw dose rates
544 have been introduced as follows:

545

546 (1) The average mean free path of alpha particles in silicates is about 20 μm .
547 Consequently, the alpha particles emitted from the uranium included in larger U-bearing
548 minerals, relatively stable under tropical weathering conditions, do not participate to the A-
549 center defects formation within the bulk kaolinite sample. To estimate the proportion of U
550 hosted in such U-bearing minerals induced-fission tracks mapping was performed on two thin
551 sections of resin embedded samples from each profile: CA 65 and CA 130, two undated blocs
552 samples representative of the top and bottom Ferralsol respectively, CO2 87 representative of
553 the Acrisol samples and another considered as representative of the bottom profile localized at
554 a depth of ca 130 cm and named after as "CO 3875".

555 The fission tracks maps show that a large part of uranium is localized in relatively scarce hot
556 spots characterizing U-bearing minerals. They can be zircon grains, characterized by stars-
557 shaped hot spots, or iron/titanium oxides, characterized by larger and more diffuse spots (see
558 Balan et al., 2005). The distribution of fission tracks through the Ferralsol profile exhibits a
559 slight decrease of U contained in U-bearing minerals from the bottom to the top of the profile
560 (Table 2 and SI 7) as 51 % of the fission tracks are contained within these minerals in the top
561 samples and 65% in the bottom samples. A similar trend is observed within the Acrisol profile
562 (CO2) (Table 3 and SI 8). The top soil samples have about 55% of uranium spread out in the
563 clayey matrix, adsorbed on phyllosilicates or oxides/oxyhydroxides and this proportion is *ca*
564 29% for the bottom samples. This suggests a dissolution/depletion of U-bearing minerals within
565 both soil horizons, as their size and number decrease from the bottom samples to the top ones.
566 Based on these observations, the dose rate was corrected by removing the alpha contribution
567 from the U contained in U-bearing minerals. It was considered that Th is distributed
568 homogeneously in the samples matrix, possibly as insoluble Th oxides (Langmuir & Herman,
569 1980), as in Balan et al. (2005) and Mathian et al. (2018). The accumulation of such Th oxides
570 in the top Acrisol profile (Th: ca 40 ppm) and at the base of the Ferralsol (Th: ca 30 ppm) may
571 explain the increase of Th content in these parts of the profiles.

572

573 (2) Laterites, and more generally soils, are open geochemical systems often characterized
574 by some disequilibrium of U and Th decay chains (Dequincey et al., 2002; Balan et al., 2005).
575 Disequilibrium can induce major changes in the total dose rate arising from uranium and
576 daughter elements (Aitken, 1985). Gamma spectrometry was performed on representative
577 samples from each profile to estimate this disequilibrium. The CA 84 sample is assumed to be
578 representative of the Ferralsol profile, CO2 200 representative of the Acrisol *solum* and
579 CO2 450 of the Acrisol saprolite. At secular, equilibrium, all radioactive elements have an

580 equivalent activity. A special attention is given to ²³⁸U and ²²²Rn activity variation within each
 581 sample because radon losses are described as one of the most current sources of disequilibrium
 582 of decay chains (Aitken, 1985; Ozkowski et al., 2000). Gamma spectrometry does not indicate
 583 radon losses but an equilibrium state for the Ferralsol (CA) sample and radon accumulation of
 584 17 and 36% for the Acrisols profile samples CO2 200 and CO2 450, respectively (Table 4).
 585 This suggests a possible recent leaching of U within the Acrisol (CO2) profile. This radon
 586 accumulation was used to correct the dose rate by adding a contribution of ²²²Rn and daughter
 587 products equivalent to its percentage of accumulation.

588

589 (3) In addition to the above correction, the water content of soil has an significant effect
 590 on the dose rate received by a soil kaolinite (Hennig et Grün, 1983; Allard, 1994). Local studies
 591 have shown that the low vertical water drainage of the Rio Negro soils is the cause of an
 592 important residence time of water in the soil (Rozanski et al., 1991). Bruno et al. (2006) have
 593 estimated average volumetric soil moisture of 0.38 m³/m³ in the dry season minimum to 0.56
 594 m³/m³ in the humid season maximum for soils of the Amazon basin. It roughly corresponds to
 595 average weighted water content of 0.2 for the local soil. The previously calculated dose rates
 596 are thus corrected using the formula of Hennig et Grün (1983).

597

$$598 \quad D_{H2O} = D\alpha \times (1 + 1.49W)^{-1} + D\beta \times (1 + 1.25W)^{-1} + D\gamma \times (1 + W)^{-1} \quad (5)$$

599 where W is a weighed water content (between 0 and 1), D_{H2O} the dose rate of the humid sample,
 600 D α , D β and D γ respectively the alpha, beta and gamma corrected dose rates of the sample.

601

602 The evolution of corrected dose rates with depth follow a different trend in each profile, (Fig.
 603 7B). In the Ferralsol profile (CA), the dose rate decreases from the bottom to the top of the
 604 saprolite (excluding the peculiar CA 480 sample) and is almost constant in the soil. The dose
 605 rate trend observed in the saprolite reflects a decrease in Th and U concentration (Fig. 7A),
 606 likely related to the dissolution of U-bearing minerals as suggested by fission tracks analyses.
 607 In the Acrisol profile (CO2), the dose rate only displays comparatively weak variations as a
 608 function of depth, excepted three Th-rich samples of the soils. The U concentration in the soil
 609 is stable and smaller than that observed in the Ferralsol, where it is also relatively stable (about
 610 1 ppm of variation). The important Th evolution in the Acrisol saprolite (about 10 ppm of
 611 variation) is linked to a lower U variation (about 3 ppm variation). It points to the fact that this
 612 saprolite is a more mature weathered material than the one of the Ferralsol, in which both U

613 and Th have an important range of evolution. These results confirm that each part of both soils
614 is not only characterized by specific mineralogy and characteristics of kaolinite but also by its
615 own geochemical dynamics.

616

617

618 **5.4 Distributions of kaolinite ages**

619

620 The kaolinite ages have been obtained as the ratio of the paleodose to the corrected dose
621 rate (Tables 2 and 3). The ages range from 0.02 Ma to 5.98 Ma. Kaolinites with ages below 0.25
622 Ma have just been indicated as “quaternary” kaolinites, owing to the large uncertainty of young
623 age (Fig. 8).

624

625 Despite different crystal-chemical characteristics, kaolinites from the two *solums* have
626 a similar age in both profiles, ranging from ca 2 Ma to 1 Ma (Fig. 8). Kaolinites from the
627 Acrisol saprolite are older (6 Ma to 3.6 Ma) than the ones from the Ferralsol saprolite (< 1 Ma).
628 It is also noteworthy that the transition between the Acrisol soil horizons and the saprolite
629 displays very recent kaolinites. It may indicate a recent activation of soil/saprolite
630 transformation front described by Nahon et al. (2003) for example. These ages are fully
631 consistent with mineralogy, geochemistry and kaolinite disorder variation: the saprolites and
632 soils are different subsystems. The kaolinites ages and their distribution in both profiles confirm
633 that they formed and evolved owing to different temporality. This supports the mineralogical
634 and geochemical results of this study, that highlight the distinction between Acrisols and
635 Ferralsols in the Curicuriari area as well as between saprolite and *solum* in each weathering
636 cover.

637 **6. Discussion**

638

639 **6.1 Weathering fronts in the investigated profiles**

640

641 The present study brings evidence that two contrasting regolith profiles contain several
642 types of kaolinites with different ages and crystal-chemical characteristics. Similar findings
643 have been reported for other laterite profiles (e.g. Balan et al., 2005; Allard et al., 2018; Mathian
644 et al., 2018). In unconsolidated tropical soils developed at the expense of kaolinite-rich
645 sediments in the Amazon basin (Lucas et al., 1987; Giral-Karmacik et al., 1998; Balan et al.,

646 2005; Balan et al., 2007), kaolinites are characterized by a decrease of the structural order and
647 particle size from the bottom to the top of the profile. This evolution was interpreted as
648 reflecting the mixing of two kaolinite generations in a proportion continuously varying with
649 depth, indicating the progressive replacement of sedimentary kaolinite by secondary kaolinites
650 along the profile due to the action of one weathering front (Balan et al., 2007).

651

652 In the present data set, the kaolinites ages in the saprolite (C horizon) of the Ferralsol
653 profile (Caju profile) tend to increase from bottom to top and attest for the recent formation of
654 kaolinite. This is consistent with the action of a vertical weathering front acting at the
655 saprolite/primary rock contact. This front may still be active, confirming that some laterites
656 profiles could also formed/evolved under the present-day climatic conditions. In contrast,
657 kaolinites ages of the Ferralsol *solum* are relatively homogeneous and older than the saprolite
658 ones. This general trend is consistent with a classical *per descensum* model of soil formation.
659 It may also be related to the concepts of soil catena (e.g. Yoo and Mudd, 2008 and references
660 therein). In this concept, soils from an hillslope are interconnected and one soil receives
661 particles from other soils upslopes but also provides particles to the soils downslopes.
662 Accordingly, a soil profile from an hillslope can be divided into an immobile part, that can
663 roughly correspond to the saprolite and the bottom part of the profile *solum*, and a mobile part
664 that can be named the “soil conveyor belt”. In this soil system, young soils particles formed at
665 the saprolite/primary rock contact move upward, in parallel of the soil formation and erosion.
666 They are then translocated downward when they reach the conveyor belt. According modelling
667 studies (see Anderson et al., 2015 for example), the particles ages within a soil profile are
668 younger and more dispersed in the bottom of this type of profile than in the conveyor belt. This
669 is consistent with the kaolinites ages organization within the ferralsol and can also explain the
670 gap of ca 0.5 Ma between the three top kaolinite samples and the ones close to *solum*/saprolite
671 transition. However, due to the location of this Ferralsol, at the top of its local slope, our data
672 do not allow one to distinguish between this model and *in situ* formation of kaolinite in the
673 Ferralsol profile without translocation of soil particles.

674 A contrario, the Acrisol (CO2 profile) displays an “inverse” kaolinite ages succession,
675 with younger kaolinites in the top soil and older in the saprolite. This age distribution may be
676 considered as characteristic of a partly rejuvenated fossilized and non active laterite profile (e.g.
677 Mathian et al., 2019). Indeed, this shows that the Acrisol *solum* formed at the expense of
678 materials weathered during a previous stage of profile development. This interpretation is
679 consistent with the stronger U depletion observed in the Acrisol profile, compared with the

680 Ferralsol. The ages trend of this profile and its location on a plateau tends to demonstrate that
681 the local Acrisol are not impacted by the presence of a soil conveyor belt. In addition, the dating
682 of secondary minerals of this profile cannot confirm the action of soil particle translocation
683 process. Absence of cutanes on soils particles in thin sections also confirms this observation.
684 Weakness of translocation evidence should be linked to local low erosion rates, low water fluid
685 horizontal circulation and to the dissolution of the oldest kaolinites of this profile.

686

687 In both profiles, the soil/saprolite transition is characterized by a relatively steep
688 variations in geochemistry and mineralogy and in characteristics of kaolinites, most especially
689 their age. This supports the idea that this transition coincides with a weathering front, as
690 suggested by Nahon (2003). In the Acrisol profile, the quaternary kaolinite age observed at the
691 soil/saprolite transition may correspond to a recent reactivation of the corresponding
692 weathering front. The presence of several generations of kaolinites within an unconsolidated
693 soil profile, demonstrated by these data and the previous EPR dating study of kaolinites (Balan
694 et al., 2005; Allard et al., 2018; Mathian et al., 2019), and their erasure or persistence linked to
695 weathering events, is a confirmation of soil polygenesis as defined by Richter and Yaalon
696 (2012). Shifting environment (climate, vegetation, hydrology) and microenvironment impacts
697 and transforms a soil profile during its life and will causes erasure of some of its features, here
698 the dissolution of kaolinite generations for example, while others are preserved. An old
699 unconsolidated soil, as the Acrisol profile presently studied, will display features characteristic
700 of the environment variations that occurred since its formation. EPR dating reveals various
701 relicts of secondary clay minerals that resisted to strong successive weathering episodes having
702 occurred since their formation. This study thus confirms that unconsolidated soils can be
703 considered as “memory of the landscape” as explained by Richter and Yaalon (2012) and
704 references.

705

706 **6.2 Relation with paleoclimates**

707

708 The presence of distinct generations of secondary minerals within a same regolith
709 indicates that several precipitation/dissolution events have affected specific parts of the profile
710 which is in line with the observations of Lucas et al. (1996) and Girard et al. (2002). Dating
711 studies of secondary minerals in laterites have shown that these phenomena are often linked to
712 the succession of specific preferential weathering periods or weathering pulses. These events
713 cause the formation of large quantity of secondary minerals that can mask or overprint the signal

714 of continuous weathering recorded within a regolith mineralogy. Relictual secondary minerals
715 (i.e. secondary minerals formed during a former weathering event preserved from the following
716 rejuvenation processes) are, in most cases, witnesses of several events (Vasconcelos, 1999;
717 Balan et al., 2005; Retallack et al., 2010; Bonnet et al., 2016; Miller et al., 2017; Allard et al.,
718 2018; Mathian et al., 2018). However, their discrete instead of continuous ages suggest that
719 they are mainly related to intense precipitation periods. During these periods, large amounts of
720 old kaolinites may be dissolved to form the observed large amount of renewed kaolinites. These
721 type of weathering events may also be linked to eustatic variations and tectonic activities that
722 can impact both continental erosion, increasing the regolith rate formation, and the watertable
723 position, acting as a local base level. The watertable is divided in two hydrological zones (Ollier
724 et al., 1988): the zone of discharge, in which the water flows and displays undersaturated
725 compositions with respect to the secondary and primary minerals, and the stagnant zone in
726 which the efficiency of primary mineral weathering is lowered because of near-equilibrium
727 conditions between minerals and aqueous solutions. The closer the watertable to the top, the
728 less the regolith volume interacts with undersaturated aqueous solutions. A contrario a
729 watertable closer to the regolith base corresponds to a larger regolith volume interacting with
730 undersaturated aqueous solutions. These phenomena should decrease or increase, respectively,
731 the vulnerability of soils to rejuvenation processes impacting their secondary minerals. Note
732 that the weathering front depth is often decoupled from the water table depth in regolith profile
733 (Braun et al., 2016). Both punctual weathering periods (i.e. precipitation related/ watertable
734 lowering related) erase the record of less intense weathering episodes, which implies that the
735 dating of kaolinite, in most cases, do not date the beginning of a profile formation.

736

737 Two main periods of formation for kaolinites have been identified (Fig. 9): ca 6-3.6 Ma,
738 in the Acrisol saprolite, and 2.5 Ma to the recent period. This last may be divided in two: 1) the
739 one ranging from 2.5 to 1 Ma for both the Acrisol and Ferralsol; 2) the one varying from ca 0.9
740 Ma to the recent periods, recorded in the Ferralsol saprolite and at the soil/saprolite transition
741 of the Acrisol profile. Both periods can be linked to major paleosurfaces identified in South
742 America using paleomagnetism and other dating methodologies used during the last three
743 decades (Bardossy and Aleva, 1990; Vasconcelos et al., 1994; Retallack, 2010; Leonardi et al.,
744 2011 and ref. therein; Monteiro et al., 2014; Allard et al., 2018; Theveniaut & Freyssinet 1999;
745 2002).

746

747 Two origins could be proposed to account for the locally observed weathering stages: 1)

748 regional climatic or geodynamic events that caused a local precipitation pulse (see Mathian et
749 al., 2019); 2) response to global water base level dropping (Haq et al., 1987) that drastically
750 increased continental erosion, and lowered the local watertable levels but could also impact a
751 larger part of the Amazon Basin. Enhanced drainage efficiency directly affects the formation
752 of regolith (Braun et al., 2016), possibly reactivating the weathering fronts in the profiles.

753

754 Concerning the first origin, several regional climatic events may coincide with the
755 formation of kaolinite generations in the studied profiles. The first weathering period, extending
756 from 6 Ma to 3.6 Ma, is recorded in the Acrisol saprolite. This generation of kaolinites may be
757 linked to the one observed in the Manaus laterites (Balan et al., 2005), as well as to some
758 duricrust samples from the Rio Negro basin (Allard et al., 2018). From a geomorphologic point
759 of view, it would be related to the end of late Velhas paleosurface of South America as defined
760 by Bardossy and Aleva (1990). The beginning of this period, younger than the pan-Amazonian
761 Ucayali Peneplain (ca 9.5/9 Ma), coincides with the last Quechua Andean uplift event (Quechua
762 III) observed in the sedimentary records by Campbell et al., (2006). The literature explained
763 that the Amazon lowland climate became humid since the Quechua I event (ca 17-15 Ma)
764 during which the Andean height (ca 2km) was sufficient to modify the air circulation over South
765 America (Campbell et al., 2006; Insel et al., 2009). No kaolinite from this period was found in
766 the studied profiles. Even if the global Earth climate was relatively cold during the Quechua III
767 period (Zachos et al., 2001), this Andean uplift has potentially influenced the intensity of the
768 rainfall in the north west of the Amazon Basin, already governed by a monsoon climate (Vonhof
769 et Kaandrop, 2010 and ref. therein). Indeed, this tectonic phenomenon was described as
770 increasing the monsoon seasonality over Amazonia by Sepulchre et al. (2010). Consequently,
771 the Acrisol saprolite kaolinite generation may result from a period of weathering intensification
772 over at least the northwestern part of Amazonia. The most recent kaolinites of this phase are
773 around 4 Ma. This period could have stopped with the potential slight fall of precipitation and
774 temperature in the Amazon basin linked to the Panama isthmus closure (Rosetti et al., 2004).
775 However, some iron oxides from duricrusts of the Curicurari and Manaus region crystallized
776 during this time period (Allard et al., 2018). These results contradict the idea of a global
777 decrease of precipitations in northwest Amazonia. The global warm period of the Mid-Pliocene
778 (ca 3.3-3 Ma, Haywood et al., 2016) is apparently not recorded in the two studied
779 unconsolidated profiles.

780

781 Two main weathering periods can be identified during the Pleistocene, one from 2.5 to 1 Ma

782 that corresponds to the formation/rejuvenation of both studied Acrisol and Ferralsol *solum* and
783 a latter one from 0.9 to the present that corresponds to the Ferralsol saprolite. The first period
784 has also been recorded within a duricrust of the Rio Negro basin (Allard et al., 2018), possibly
785 formed during a base level dropping as it is today located below the river level. The second
786 Pleistocene weathering period (less than 1 Ma) has also been identified in Amazonia by
787 Vasconcelos et al. (1994). Both periods can be correlated with the Quaternary Paraguaçu
788 weathering surface (King, 1956; Bardossy and Aleva, 1990). No regional geodynamic-linked
789 climatic events can be linked with these preferential periods of weathering. However, the
790 Amazonian climate since the Miocene, and particularly during the Quaternary, was dependent
791 on the Intertropical convergence zone migration (Harris & Mix, 1999; Vonhof & Kaandrop,
792 2010). The ICTZ position depends on Milankovitch cycles and is accordingly linked to global
793 Earth climate. Aris & Mix (1999) explained that the ICTZ migration through the Quaternary
794 has caused a succession of arid climates in Amazonia during the ice age periods, and hot and
795 warm climate during the interglacial periods. Consequently, the quaternary kaolinites from both
796 profiles may have developed through these last humid periods. However, due to its limited
797 precision, the EPR dating methodology cannot precisely identify their succession.

798

799 Concerning the second hypothesis, several important global sea level falls have been observed
800 since 10 Ma by Haq et al. (1987) and Miller et al. (2005). These events will be reflected on the
801 continent by a global base level dropping that likely caused the lowering of the Curicuriari
802 watertable depth and also increase the regional erosion. Even if 7 sea levels events (ca 8 Ma,
803 6.2 Ma, 5.5 Ma, 4 Ma, 3 to 2 Ma, 1.5 Ma and 1 to actual Ma) have been recorded within
804 sedimentary basin by Haq et al. (1987), it is difficult to compare the ages of both profiles
805 rejuvenation episodes to a precise event of this kind. Indeed, the speed of upstream advance of
806 incision waves from the Atlantic ocean to the upper Amazon lowland is unknown. However,
807 the influence of these events on the birth and propagation of secondary weathering fronts must
808 be considered. Thus, the modern incision trend of the plateaus edges, allowing the Ferralsol
809 (CA) development, could also be a response to the last sea level drop (ca 100ka, Miller et al.
810 2005) impacting the Curicuriari region base level. A contrario, the direct impact of the Andean
811 uplift on the local base level (watertable depth and rivers level) appears as less likely due to the
812 distance between the Curicuari basin and the Andes. However, it caused the development of
813 the modern Amazon drainage system at the Late Miocene and beginning of Pliocene (see Mora
814 et al., 2010 and references). The development of this erosional system and its change on the
815 local hydrology, may also be correlated to the initial formation of the Acrisol saprolite found

816 on the Curicuriari plateaus.

817

818 **6.3 The Ferralsol/Acrisol transition**

819

820 The present study highlights major differences between the Acrisol and the Ferralsol. The
821 yellowish Acrisol contains kaolinite and goethite from the bottom to the top profile but the
822 kaolinite content decreases in the soil toward the surface. This clay depletion is a major step for
823 Acrisol formation in former models of weathering covers evolution in the Amazon Basin
824 (Fritsch et al 2011; Melfi et al. 1996). By contrast, the mineralogical evolution of the Ferralsol
825 can be described by a kaolinite accumulation from the top saprolite to the top soil. Indeed, early
826 products of weathering formed in this profile are gibbsite and hematite, that indicates a high
827 and low water activity in the soil, respectively (Beauvais et Tardy, 1991; Beauvais et al., 2009).
828 The presence of gibbsite as one of the earliest secondary minerals can be considered as a
829 common feature during the weathering of well-drained Al-rich rocks, forming fluids easily
830 saturated with respect to gibbsite, (Anand et al., 1985; Herrmann et al., 2007; Shvartsev, 2012)
831 and has also been observed in other sites from Brazil (Dubroeuq and Volkoff, 1988; Lucas et
832 al., 1996; Furian et al., 2001). Gibbsite is then replaced by kaolinite in the top profile, probably
833 linked to quartz dissolution, as suggested by the Si geochemical trend (SI 3) and a lower water
834 activity in the top profile.

835 Kaolinites in the Ferralsol and Acrisol soils have similar ages. Accordingly, no data of
836 this study support the idea of the local transformation of the present day Ferralsol into the
837 Acrisol, as could eventually be expected in a context of a “yellowing front” as was observed in
838 the Manaus area (Fritsch et al., 2011). This process, a transformation of a red Ferralsol toward
839 a yellow one, was interpreted as a vertical mineralogical transformation within a profile due to
840 the present days warm and humid climate. Based on the chronology established in the present
841 study, both type of *solum* could correspond to the same weathering events having affected
842 different types of materials: weathered materials, preserved in its saprolite, for the Acrisol and
843 fresher rock for the Ferralsol. This interpretation is consistent with the occurrence of Ferralsols
844 on incised plateau edge, favoring the erosion of ancient weathering products along the slope
845 and valley. These ages are consistent with the local geomorphological observations (Taitson
846 Bueno, 2009) showing the extension of recent Ferralsol domains at the expense of older
847 Acrisols in parallel of plateau erosion. In this case, erosion and quaternary weathering of fresh
848 rock tends to be the main process guiding the replacement of Acrisol by Ferralsol. However, a
849 lower elevation of the Ferralsol derived from fresh rock could be expected. In addition, our

850 mineralogical and kaolinite dating data cannot confirm the idea that the local Ferralsol *solum*
851 replace Acrisol *solum* due to a desilification process affecting the kaolinite as both have
852 kaolinite with a similar age.

853 An alternative scenario can be proposed from the age organization and mineralogy of
854 both profiles. Indeed, gibbsite, is present in low amount in the Acrisol *solum* and in increasing
855 amounts from the Ferralsol *solum* to the Ferralsol saprolite. It can suggest a mineralogical and
856 geochemical filiation between the two profiles. In this case, the original material of the present
857 day Ferralsol profile and Acrisol *solum* could be the relictual Acrisol saprolite that covered the
858 plateau. This saprolite was submitted, during the Quaternary, to an intense weathering episode
859 that continued until present time on the incised edges of the plateau, and transformed its parent
860 material at least on 5m deep, because of increased drainage conditions. On the plateau, this
861 weathering front exists also between the *solum* and the saprolite of the Acrisol, albeit with
862 limited extent: it may be delayed, owing to unfavourable drainage conditions produced by the
863 clay-rich horizons. In this scenario, rejuvenation of older kaolinite generations is central and
864 relies on the modification of the hydrological properties of the profiles together with
865 progressive Si leaching and erosion. Consistently, the Si content in the Ferralsol is 10 to 20%
866 lower than in the Acrisol.

867 In the Curicuriari Basin, both Ferralsol and Acrisol can be replaced by Podzols which are
868 observed to form at the center of the plateaus over the inundated plains and depressions
869 (Dubroeuq et Volkoff, 1998; Do Nascimento et al., 2004; Fritsch et al, 2011 and ref. therein;
870 Ishida et al., 2014) and over the slopes of river incisions (Lucas et al., 1996). Moreover, it is
871 not excluded that the transformation of an old Ferralsol into the present-day Acrisol, described
872 in the model of Taitson Bueno (2009), occurred earlier than 6 Ma. However, our study did not
873 reveal relictural parts of tertiary ferralsols within the Acrisol.

874 **7. Conclusion**

875
876 This study provides new absolute ages kaolinite formation in Acrisol and Ferralsol, that
877 belong to common weathering covers in the upper Amazon Basin. Both types of soils are the
878 result of different processes linked to the topography evolution and possibly to their respective
879 soil drainage conditions. The present data set confirms and specifies the initial
880 geomorphological model by Taitson Bueno (2009). It also confirms that soil and saprolite are
881 distinct systems, owing to their mineralogy, crystal chemistry and ages of kaolinites.

882

883 Following previous dating studies of laterites, this study shows that unconsolidated
884 lateritic profiles contain several generations of kaolinite that have recorded the signature of
885 discrete preferential weathering periods consistent with climatic variations. At least 3 events
886 are recognized: one recorded in the Acrisol saprolite between ca 6-3.6 Ma, one that renewed
887 the Acrisol *solum* and potentially triggered the Ferralsol formation between 2.5 to ca 1 Ma and
888 a last event that is only revealed in the Ferralsol saprolite between 1 Ma and present. The
889 recorded weathering periods coincide with major paleoclimatic events. The first weathering
890 period may have been triggered by the impact of Quechua III event on Amazonian monsoonal
891 system and may have stopped after an aridification of this region linked to the impact of the
892 Panama closure on climate. The two others might result from ITCZ migration due to
893 Milankovitch cycles succession. The influence of variation of water base level may also be
894 relevant, but it is difficult to establish owing to the insufficient precision of EPR ages. In line
895 with other dating studies, these results confirm that upper Miocene to Quaternary periods were
896 favourable to the laterite development over the Amazon basin.

897

898 **Acknowledgements**

899

900 Support by M. Guillaumet, L. Delbes, K. Béneut and the IMPMC spectroscopy and XRD
901 platforms is acknowledged. We thank the anonymous reviewers for their pertinent comments.

902

903

904 **Bibliography**

905

- 906 Aitken, M.J. (1985) Thermoluminescence dating. Studies in archaeological science. *Academic Press, London* (359
907 pp).
- 908 Allard, T., Muller, J.P., Dran, J.C., Ménager, M.T. (1994) Radiation-induced paramagnetic defects in natural
909 kaolinites : alpha dosimetry with ion beam irradiation, *Physics and chemistry of minerals*, 85-96.
- 910 Allard, T., Balan, E., Calas, G., Fourdrin, C., Morichon, E., Sorieul, S. (2012) Radiation induced defects in clay
911 minerals : A review, *Nuclear Instruments and methods in physics research*, 112-120.
- 912 Allard, T., Gautheron, C., Riffel, S.B., Balan, E., Soares, B.F., Pinna-Jamme, R., Derycke, A., Morin G., Bueno,
913 G.T., do Nascimento, N. (2018) Combined dating of goethites and kaolinites from ferruginous duricrusts.
914 Deciphering the Late Neogene erosion history of Central Amazonia, *Chemical Geology*, **479**, 136-150.
- 915 Almeida, M.E. (2005) Reconhecimento geológico ao longo do baixo curso do rio Curicuriari, noroeste do Estado
916 do Amazonas, *CRPM*.
- 917 Anand, R.R., Gilkes, R.J., Armitage, T.M., Hillyer, J.W. (1985) Feldspar weathering in lateritic saprolite, *Clays
918 and Clay Minerals*, **33** (1); 31-43.
- 919 Anderson et al. (2015) Particle trajectories on hillslopes: Implications for particle age and ¹⁰Be structure. *Journal
920 of Geophysical Research: Earth Surface*, **120**, 1626-1644.
- 921 Angel, B.R., Jones, J.P.E., Hall, P.L. (1974) Electron spin resonance studies of doped synthetic Kaolinite I. *Clay
922 Minerals*, **10**, 247-255.
- 923 Balan, E., Allard, T., Boizot, B., Morin, G., Muller, J.P. (1999) Structural Fe³⁺ in natural kaolinites: new insights
924 from electron paramagnetic resonance spectra fitting at X and Q-band frequencies. *Clays and Clay Minerals*,
925 **47** (5), 605-616.

- 926 Balan, E., Allard, T., Boizot, B., Morin, G., Muller, J.P. (2000) Quantitative measurement of paramagnetic Fe³⁺
927 in kaolinite. *Clay and Clay minerals*, **48** (4), 439-445.
- 928 Balan, E., Saitta, A.M., Mauri, F., Calas, G. (2001) First-principles modeling of the infrared spectrum of kaolinite,
929 *American Mineralogist*, **86**, 1321-1330.
- 930 Balan, E., Fritsch, E., Allard, T. & Calas, G. (2005) Formation and evolution of lateritic profiles in the middle
931 Amazon basin : Insights from radiation-induced defects in kaolinite, *Geochimica and Cosmochimica Acta.*, **69**
932 (9), 2193-2204.
- 933 Balan, E., Lazzeri, M., Morin, G., Mauri, F. (2006) First-principles study of the OH stretching modes of gibbsite.
934 *American Mineralogist*, **91**, 115-119.
- 935 Balan, E., Fritsch, E., Allard, T. & Calas, G. (2007) Inheritance vs. Neof ormation of kaolinite during lateritic soil
936 formation : a case study in the middle Amazon Basin. *Clays and Clay minerals*, **55** (3), 253-259.
- 937 Balan, E., Delattre, S., Guillaumet, M., Salje, E. (2010) Low-Temperature infrared spectroscopic study of OH-
938 stretching modes in kaolinite and dickite. *American Mineralogist*, **95** (8-9), 1257-1266.
- 939 Bardossy, G., Aleva, G.J.J. (1990) Lateritic bauxites. *Dev. Econ. Geol.*, **27**, 624.
- 940 Bartoli, G., Sarnthein, M., Weinelt, M., Erlenkeuser, H., Garbe-Schönberg, D., Lea, D.W. (2005) Final closure of
941 Panama and the onset of northern hemisphere glaciation. *Earth and Planetary Science Letters*, **237**, 33-44.
- 942 Beauvais, A., Tardy, Y. (1991), Formation et dégradation des cuirasses ferrugineuses sous climat tropical humide,
943 à la lisière de la forêt équatoriale. *Comptes Rendus de l'Académie des Sciences, Séries II* **13**, 1539-1545
- 944 Beauvais, A., Ruffet, G., Hénocque, O., Colin, F. (2008) Chemical and physical erosion rhythms of the West
945 African Cenozoic morphogenesis: the ⁴⁰Ar-³⁹Ar of supergene K-Mn oxides. *Journal of Geophysical Research*,
946 **113**, F04007.
- 947 Beauvais, A. (2009) Ferricrete biochemical degradation on the rainforest–savannas boundary of Central African
948 Republic. *Geoderma*, **150**, 379-388.
- 949 Billups, K., Ravelo, A.C., Zachos, J.C., Norris, R.D. (1999) Link between oceanic heat transport, thermohaline
950 circulation and the Intertropical Convergence Zone in the early Pliocene Atlantic. *Geology*, **27**, 319-322.
- 951 Bland W., Rolls D (1998) Weathering: An introduction to the scientific principles. *London: Routledge*, 288
- 952 Bonnet, N.J., Beauvais, A., Arnaud, N., Chardon, D., Jayananda, M. (2016), Cenozoic lateritic weathering and
953 erosion history of Peninsular India from ⁴⁰Ar/³⁹Ar dating of supergene K-Mn oxides, *Chemical Geology*, **446**,
954 33-53.
- 955 Bookhagen, B., Strecker, M.R. (2010). Modern Andean rainfall variation during ENSO cycles and its impact on
956 the Amazon drainage basin. *Amazonia, Landscape and Species Evolution: A look into the Past.*, **1 st edition**.
957 Edited by C. Hoorn and F.P. Wesselingh, Chapter thirteen.
- 958 Bookhagen, B., Strecker, M.R. (2008). Orographic barriers, high resolution TRMM rainfall, and relief variations
959 along the eastern Andes. *Geophys. Res. Lett.*, **33**
- 960 Braun, J., Mercier, J., Guillocheau, F., Robin, C. (2016) A simple model for regolith formation by chemical
961 weathering. *Journal of Geophysical Research: Earth Surface*, **121** (11), 2140-2171
- 962 Bruno, R.D., da Rocha, H.R., de Freitas, H.C., Goulden, M.L., Miller, S. (2006) Soil moisture dynamics in an
963 eastern Amazonian tropical forest. *Hydrological Processes*, **20**, 2477-2489.
- 964 Calas, G. (1988) Electron Paramagnetic Resonance. *Rev. Mineral*, **18**, 513-571.
- 965 Campbell, K.E. Jr.; Frailey, C.D.; Romero-Pittman, L. (2006) The Pan-Amazonian Ucayali Peneplain, late
966 Neogene sedimentation in Amazonia, and the birth of the modern Amazon River system. *Palaeogeography,*
967 *Palaeoclimatology, Palaeoecology*, **239**, 166-219.
- 968 Chauvel, A., Pedro, G. (1978) Genèse de sols beiges (ferrugineux tropicaux lessivés) par transformation des sols
969 rouges (ferrallitiques) de Casamance (Sénégal) modalité de leur propagation. *Cah. ORSTOM sér. Pédol.*, **16**
970 (3), 231-249
- 971 Clozel, B., Allard, T., Muller, J.P. (1994) Nature and stability of radiation-induced defects in natural kaolinites :
972 new results and a reappraisal of published works. *Clay and Clay Minerals*, **42** (6), 657-666.
- 973 Cramer, B.S., Toggweiler, J.R., Wright, J.D., Katz, M.E., Miller, K.G. (2009) Ocean overturning since the Late
974 Cretaceous: Inferences from a new benthic foraminiferal isotope compilation. *Paleoceanography*, **24**,
975 4216
- 976 Dall'agnol R., Macambira M.J.B. (1992) Titanita-biotita granitos do Baixo Rio Uaupés, Província Rio Negro,
977 Amazonas. Parte I: Geologia petrografia e geocronologia. *Rev. Bras. Geoc.*, **22**, 3-14.
- 978 Dequincey, O., Chabaux, F., Clauer, N., Sigmarrsson, O., Liewig, N., Leprun, J.C. (2002) Chemical obilizations in
979 laterites: evidence from trace elements and ²³⁸U-²²³U-²³⁰Th disequilibria. *Geochimica et Cosmochimica Acta*,
980 **66** (7), 1197-1210.
- 981 Do Nascimento, N.R., Bueno, G.T., Fritsch, E., Herbillon, A.J., Allard, T., Melfi, A.J., Astolfo, R., Boucher, H.,
982 Li, Y. (2004) Podzolisation as a deferralitization process. A study of an Acrisol-Podzol sequence de- rived
983 from Paleozoic sandstones in the northern upper Amazon Basin. *European Journal of Soil Science*, **55**, 523–
984 538.

- 985 Dubroeuq, D. Volkoff, B. (1988) Evolution des couvertures pédologiques sableuses à podzols géants
986 d'Amazonie, bassin du haut Rio Negro. *Cah. ORSTOM sér. Pédol.*, **24 (3)**, 191-214
987 Dubroeuq, D. Volkoff, B. (1998) From oxisols to Spodosols and Histosols: evolution of the soil mantles in the
988 Rio Negro basin (Amazonia). *Catena*, **32**, 245-280
989 Duval, M., (2012) Dose response curve of the ESR signal of the Aluminium center in quartz grains extracted from
990 sediment. *Ancient TL*, **30**, 41-49.
991 FAO Unesco (1998) Soil Map of the world
992 Farmer, V.C. (1974) The layer silicates. *The infrared spectra of minerals*, The mineralogical society, **4**, 331-363
993 Fritsch, E., Herbillon, A.J., Jeanroy, E., Pillon, P., Barres, O. (1989) Variations minéralogiques et structurales
994 accompagnant le passage « sols rouges – sols jaunes » dans un bassin versant caractéristique de la zone de
995 contact forêt-savane de l'Afrique occidentale (Booro-Borotou, Côte d'Ivoire). *Science Géologiques, bulletins
996 et mémoires*, **42 (2)**, 65–89.
997 Fritsch, E., Montes-Lauar, C.R., Boulet, R., Melfi, A.J., Balan, E., Magat, P. (2002) Lateritic and redoximorphic
998 features in fractured soils and sediments of the Manaus plateaus, Brazil. *European Journal of Soil Science*, **53**,
999 203–218.
1000 Fritsch, E., Morin, G., Bedidi, A., Bonnin, D., Balan, E., Caquineau, S. & Calas, G. (2005) Transformation of
1001 haematite and Al-poor goethite to Al-rich goethite and associated yellowing in a ferralitic clay soil profile of
1002 the middle Amazon Basin (Manaus, Brazil). *European Journal of Soil Science*, **56**, 575–588.
1003 Fritsch, E., Balan, E., Régina Do Nascimento, N., Allard, T., Bardy, M., Bueno, G., Derenne, S., Melfi, A.J. &
1004 Calas, G. (2011) Deciphering the weathering processes using environmental mineralogy and geochemistry:
1005 Towards an integrated model of laterite and podzol genesis in the Upper Amazon Basin. *Comptes Rendus
1006 Geoscience*, **343**, 188–198.
1007 Furian, S., Barbiero, L., Boulet, R., Curmi, P., Grimaldi, M., Grimaldi, C. (2001) Distribution and Dynamic of
1008 Gibbsite and Kaolinite in an Oxisol of Serra do Mar, southeastern Brazil. *Geoderma*, **106**, 83-100.
1009 Gaillardet, J., Dupre, B., Allegre, C.J., Négrel, P. (1997) Chemical and physical denudation in the Amazon River
1010 Basin. *Chemical Geology*, **142 (3-4)**, 141-173.
1011 Gaite, J.M., Ermakoff, P. Allard, T., Muller, J.P. (1997) Paramagnetic Fe³⁺: A sensitive probe for disorder in
1012 kaolinite. *Clay and clay minerals*, **45**, 496-505.
1013 Gehring, A.U., Fry, I.V., Luster, J. Sposito, G. (1993), The chemical form of Vanadium (IV) in Kaolinite. *Clay
1014 Minerals*, **41 (6)**, 662-667.
1015 Giral-Kacmarcik, S., Savin, S.M., Nahon, D.B., Girard, J.-P., Lucas, Y. & Abel, L.J. (1998) Oxygen isotope
1016 geochemistry of kaolinite in laterite-forming processes, Manaus, Amazonas, Brazil. *Geochimica et
1017 cosmochimica acta*, **62**, 1865–1879.
1018 Girard, J.-P., Freyssinet, P. & Morillon, A.-C. (2002) Oxygen isotope study of Cayenne duricrust paleosurfaces:
1019 implications for past climate and laterization processes over French Guiana. *Chemical Geology*, **191**, 329–343.
1020 Hall, P.L. (1980) The application of electronic paramagnetic resonance spectroscopy to studies of clay minerals:
1021 I. Isomorphous substitutions and external surface properties. *Clay Minerals*, **15**, 321-335.
1022 Haq, B. U., Hardenbol, Vail, J.P. (1987) Chronology of Fluctuating Sea Levels Since the Triassic. *Science*, **235**,
1023 1156-1166.
1024 Harris, S.E., Mix, A.C. (1999) Pleistocene precipitation balance in the Amazon basin recorded in deep sea
1025 sediments. *Quaternary Research*, **51**, 14-26.
1026 Haywood, A.M., Dowsett, H.J., Dolan, A.M. (2016) Integrating geological archives and climate models for the
1027 mid-Pliocene warm period. *Nature Communication*, **7**: **10646**, 2-14.
1028 Hennig, G.J., Grün, R. (1983) ESR dating in quaternary geology. *Quaternary Science Review*, **2**, 157-238.
1029 Hermann, L., Anongrak, N., Zarei, M., Schuler, U., Spohrer, K. (2007) Factors and processes of gibbsite formation
1030 in Northern Thailand, *Catena*, **71**, 279-291.
1031 Hoorn, C., Wesselingh, F.P., ter Steege, H., Bermudez, M.A., Mora, A., Sevink, J., Sanmartin, I., Sanchez-
1032 Meseguer, A., Anderson, C.L., Figueiredo, J.P., Jaramillo, C., Riff, D., Negri, F.R., Hooghiemstra, H.,
1033 Lundberg, J., Stadler, T., Särkinen, T., Antonelli, A. (2010) Amazonia Through Time: Andean Uplift, Climate
1034 Change, Landscape Evolution and Biodiversity. *Science*, **330**, 927.
1035 Hovan, S. (1995) Late Cenozoic atmospheric circulation intensity and climate history recorded in eolian deposits
1036 in the eastern equatorial Pacific. *Proceeding of Ocean Drilling Program*, **138**, 615-625.
1037 Insel, N., Poulsen, C.J., Ehlers, T.A. (2009) Influence of the Andes Mountains on South American moisture
1038 transport, convection and precipitation. *Clim. Dyn.*, **35 (7-8)**, 1477-1492.
1039 Ishida, D.A., Montes, C.R., Lucas, Y., Pereira, O.J.R., Merdy, P., Melfi, A.J. (2014) Genetic relationships between
1040 ferralsols, podzols and white kaolin in Amazonia. *European Journal of Soil Science*, **65**, 706-717.
1041 Karas, C., Nürnberg, D., Bahr, A., Groeneveld, J., Herrle, J.O., Tiedemann, R., deMenocal, P. (2017). Pliocene
1042 oceanic seaways and global climate. *Sci. Rep.*, **7**, **39842**
1043 King, L.C. (1956) Geomorfologia do Brazil Oriental. *Rev. Bras. Geografia*. **18 (2)**, 146-265

- 1044 Kleeman, J.D., Lovering, J.F. (1967) Uranium distribution in rocks by fission-track registration in lexan plastic.
 1045 *Science*, **156 (3774)**, 512-513.
- 1046 Langmuir, D., Herman, J.S. (1980) The mobility of thorium in natural waters at low temperatures. *Geochimica et*
 1047 *Cosmochimica Acta*, **44**, 1753-1766.
- 1048 Leonardi, F.A.; Ladeira, F.S.B. (2011) Santos, M. Paleosurfaces and Bauxite Profiles in the Poços de Caldas
 1049 Plateau, São Paulo/Minas Gerais, Brazil. *Geociências*, **30 (2)**, 147-160.
- 1050 Linton, D.L. (1955) The problem of tors. *The Geographical Journal*, **121(4)**, 470-481
- 1051 Lucas, Y., Boulet, R. et Veillon, L. 1987. Systèmes sols ferrallitiques - podzols en région amazonienne. *Podzols et*
 1052 *Podzolisation*, Righi, D. et Chauvel, A., éd. INRA, Paris, 53-65.
- 1053 Lucas, Y., Nahon, D., Cornu, S., Eyrolle, F. (1996) Genèse et fonctionnement des sols en milieu équatorial.
 1054 *Compte Rendus de l'Académie des Sciences*, **322**, 1-16.
- 1055 Lucas, Y., Montes, C.R., Mounier, S., Loustau Cazalet, M., Ishida, D., Achard, R., Garnier, C., Coulomb, B.,
 1056 Melfi, A.J. (2012) Biogeochemistry of an Amazonian podzol-ferralsols soil system with white kaolin.
 1057 *Biogeosciences*, **9**, 3705-3720.
- 1058 Maignien, R. (1961) Le passage des sols ferrugineux aux sols ferrallitiques dans les régions sud-ouest du Sénégal
 1059 (République du Sénégal). *Sols africains*, **6 (2 et 3)**, 113-228
- 1060 Mathian, M., Aufort, J., Braun, J.J., Riotte, J., Selo, M., Balan, E., Fritsch, E., Bhattacharya, S., Allard, T. (2018)
 1061 EPR dating of laterites from Western Ghats (India): a record of Asiatic monsoon strengthening. Submitted in
 1062 Gondwana Research.
- 1063 Mehra, O.P., Jackson, M.L. (1960) Iron oxide removal from soils and clays by a dithionite-citrate system buffered
 1064 with sodium bicarbonate. *Clays and Clay minerals*, **7**, 317-327.
- 1065 Melfi, A., Fritsch, E., Boulet, R., Seyler, F., Carvalho, A., Magat, P. (1996) Magat, P. In Distribuição dos solos
 1066 nas paisagens lateríticas da amazônia. Elaboração de um modelo conceitual ilustrando a evolução hydro-bio-
 1067 geoquímica destas paisagens, XIII Congresso Latino Americano de Ciência do solo, Águas de Lindoia, Brasil
- 1068 Miller, K.G., Kominzs, M.A., Browning, J.V., Wright, J.D., Mountain, G.S., Katz, M.E., Sugarman, P.J., Cram,
 1069 B.S., Christie-Blick, N., Pekar, S.F. (2005) The Phanerozoic Record of Global Sea-Level Change. *Science*,
 1070 **310**, 1293-1298.
- 1071 Monteiro, H.S., Vasconcelos, P.M., Farley, K.A., Spier, C.A., Mello, C.L. (2014) (U–Th)/He geochronology of
 1072 goethite and the origin and evolution of cangas. *Geochimica Cosmochimica Acta*, **131**, 267-289.
- 1073 Montes, C., Cardona, A., Jaramillo, C., Pardo, A., Silva, J.C., Valencia, V., Ayala, C., Pérez-Angel, L.C.,
 1074 Rofriguez-Parra, L.A., Ramirez, V., Nino, H. (2015) Middle Miocene closure of the Central American Seaway.
 1075 *Science*, **348**, 226-229.
- 1076 Mora, A., Baby, P., Roddaz, M., Parra, M., Brusset, S., Hermoza, W., Espurt, N. (2010) Tectonic history of the
 1077 Andes and Sub-Andean zones: implications for the development of the Amazon drainage basin. *Amazonia,*
 1078 *Landscape and Species Evolution: A look into the Past.*, **1 st edition**. Edited by C. Hoorn and F.P. Wesselingh,
 1079 Chapter four.
- 1080 Mosser, C., Boudeulle, M., Weber, F., Pacquet, A. (1996) Ferriferous and vanadiferous kaolinites from the
 1081 hydrothermal alteration halo of the Cigar Lake uranium deposit (Canada). *Clay Minerals*, **32**, 291-299.
- 1082 Muller, J.P., Calas, G. (1993) Genetic significance of paramagnetic centers in kaolinites. *Kaolin Genesis and*
 1083 *Utilization*, HH. Murray, W. Bundy and C. Harvey, eds, The Clay Minerals Society, Boulder, Colorado, 261-
 1084 289.
- 1085 Nahon, D. (2003) Altérations dans la zone tropicale. Signification à travers les mécanismes anciens et/ou encore
 1086 actuels. *C.R. Geosciences*, **335**, 1109-1119.
- 1087 Oczkowski, H.L., Prezegietka, K.R., Lankauf, K.R., Szmanda, J.B. (2000) Gamma spectrometry in
 1088 thermoluminescence dating. *Geochronometria*, **18**, 57-62
- 1089 Ollier et al., 1988
- 1090 Premović P.I., Ilić B.S. & Djordjević D.M. (2011) A new method for determining the concentration of vanadyl
 1091 ions in clays. *Geol. Carpathica*, **62**, 181-186.
- 1092 Price, P.B., Walker, R.M. (1963) Fossil tracks of charged particles in mica and the age of minerals. *Journal of*
 1093 *geophysical research*, **68 (16)**, 4847-4862.
- 1094 Projeto Radam (or Radam Brazil) 1972–78. Levantamento de Recursos Naturais. Ministerio das Minas e Energia,
 1095 Departamento Nacional da Produca o Mineral, Rio de Janeiro, Brazil.
- 1096 Richter, D.deB., Yaalon, D.H. (2012) “The Changing Model of Soil” Revisited. *Soil Science Society of America*
 1097 *Journal*, **76**, 766-778.
- 1098 Rossetti, D.d.F., de Toledo, P.M., Goes, A.M. (2005) New geological framework for Western Amazonia (Brazil)
 1099 and implications for biogeography and evolution. *Quaternary Reseach*, **63**, 78-89.
- 1100 Rozanski, K. Araguas-Aruaguas, L., Plata, B.A., Franken, W., Tancredi, A.C., Tundis Vital, A. (1991) Downward
 1101 movement of soil moisture in the central Amazon region traced by means of hydrogen isotopes. *Proc.*
 1102 *International Symposium on the use of stable isotopes in Plant nutrition, soil fertility and environmental study,*
 1103 **IAEA-SM-313**.

- 1104 Santos J.O.S, Hartmann L.A., Gaudette H.E., Groves D.I., Mc Naughton N.J., Fletcher I.R. (2000) A new
 1105 understanding of the provinces of the Amazon Craton based on integration of field mapping and U-Pb and Sm-
 1106 Nd geochronology. *Gondwana Research*, **3** (4), 453-488
- 1107 Sélo, M. (1983) La fission nucléaire et sa signification en géochronologie, paléothermométrie et géochimie.
 1108 Applications à l'étude particulière des basalts océaniques. Thèse d'état, Université Paris VI.
- 1109 Sepulchre, P., Sloa, L.C., Fluteau, F. (2010). Climate variation in Amazonia during the Neogene and the
 1110 Quaternary. *Amazonia, Landscape and Species Evolution: A look into the Past.*, **1 st edition**. Edited by C.
 1111 Hoorn and F.P. Wesselingh, Chapter thirteen.
- 1112 Schwertmann, U. (1993) Relations between iron oxides, soil color and soil formation. *Soil color*, J.M. Bogham
 1113 and E.J. Ciolkosz, editors, SSSA, Madison, WI, 51-69
- 1114 Shvartsev, S.L. (2012) The Internal Evolution of the Water-Rock Geological System. *Herald of the Russian
 1115 Academy of Soil Sciences*, **82**, 134-142.
- 1116 Shuster, D.L., Vasconcelos, P.M., Heim, J.A., Farley, K.A. (2005) Weathering geochronology by (U-Th)/He
 1117 dating of goethite. *Geochimica et Cosmochimica Acta*, **69**(3), 659-673.
- 1118 Taitson Bueno, G. (2009) Podzolização das lateritas da alta bacia amazônica: Mecanismos, características
 1119 mineralógicas dos produtos neoformados e relações com a evolução da paisagem. PhD of Universidade Estadual
 1120 Paulista Júlio de Mesquita Filho, UNESP, Brasil.
- 1121 Taitson Bueno, G., Soares Cherem, L.F., Toni, F., Silva Guimarães, F., Bayer, M. (2019) Amazonia. *The
 1122 physical Geography of Brazil, Geography of the physical environment*, eds A.A.R. Salgado et al.
- 1123 Tardy, Y., Kobilsek, B., Paquet, H. (1991) Mineralogical composition and geographical distribution of African
 1124 and Brazilian periatlantic laterites. The influence of continental drift and tropical paleoclimate during the past
 1125 150 million years and implications for India and Australia, *Journal of African Earth Sciences*, **12**, 283-295
- 1126 Taylor, R.G., Howard, K.W.F. (1999) Lithological evidence for the evolution of weathered mantles in Uganda by
 1127 tectonically controlled cycles of deep weathering and stripping. *Catena*, **35**, 65-94.
- 1128 Théveniaut, H., Freyssinet, P. (1999) Paleomagnetism applied to lateritic profiles to assess saprolite and duricrust
 1129 formation processes: the example of Mont Baduel profile (French Guiana). *Palaeogeogr., Palaeoclim.,
 1130 Palaeoecol.*, **148** (4), 209-231.
- 1131 Théveniaut, H., Freyssinet, P. (2002) Timing of lateritization on the Guiana Shield: synthesis of paleomagnetic
 1132 results from French Guiana and Suriname. *Palaeogeogr., Palaeoclim., Palaeoecol.*, **178** (1-2), 91-117.
- 1133 Retallack, G.J. (2010) Lateritization and bauxitization events. *Economic Geology*, **105**, 655-667.
- 1134 Russel, J.D., Fraser, A.R. (1994) Infrared methods. Clay mineralogy: Spectroscopic and Chemical Determinative
 1135 methods, London: Chapman et al., 11-67
- 1136 Vasconcelos, P.M., Renne, P.R., Brimhall, G.H., Becker, T.A. (1994) Direct dating of weathering phenomena by
 1137 ⁴⁰Ar/³⁹Ar and K-Ar analysis of supergene K-Mn oxides. *Geochimica et Cosmochimica Acta*, **6**, 1635-1665.
- 1138 Vasconcelos, P.M. (1999) K-Ar AND ⁴⁰Ar/³⁹Ar Geochronology of weathering processes. *Annual Review of Earth
 1139 and Planetary Science*, **27**, 183-229.
- 1140 Vasconcelos, P.M., Reich, M., Suster, D.L., (2015). The paleoclimatic signatures of supergene metal deposits.
 1141 Elements, 11, 317-322.
- 1142 Vonhof, H.B., Kaandorp, R.J.G. (2010). Climate variation in Amazonia during the Neogene and the Quaternary.
 1143 *Amazonia, Landscape and Species Evolution: A look into the Past.*, **1 st edition**. Edited by C. Hoorn and F.P.
 1144 Wesselingh, Chapter twelve.
- 1145 Yoo, K., Mudd, S.M. (2008). Toward process-based modeling of geochemical soil formation across diverse
 1146 landforms: A new mathematical framework. *Geoderma*, **146**, 248-260.
- 1147 Zachos, J., Pagani, M., Sloan, L., Thomas, E., Billups, K. (2001) Trends, Rhythms, and Aberrations in Global
 1148 Climate 65 Ma to Present. *Science*, **292**, 686-693.

1149
 1150

1151 **Figures captions:**

1152
 1153 **Fig. 1: A:** Soil map of Amazonia (modified from Taitson et al., 2019) and approximative location of the region
 1154 study **B:** Soil map of the Rio Curicuriari basin, with the several soils transitions linked to the topography. **C:**
 1155 Schematic geomorphologic model of local soil landform dynamic with their three major weathering and erosion
 1156 processes: podzolisation (white arrow), iron and clay translocation (Acrisol formation, grey arrow) and river
 1157 network incision (dark arrow). The Ib and Ic sequence are characteristic of low and middle Rio Negro catchment
 1158 and IIb and IIc of the Upper Rio Negro catchment. The Rio Curicuriari studied transect is characteristic of the Ib
 1159 scheme (From Bueno Taitson, 2009).

1160
1161 **Fig. 2:** Scheme of the Caju (CA)-Cobra (CO2) transect, with the lateral transformation of Acrisol into Podzol and
1162 the Ferralsol/Acrisol transition. Two profiles, Caju and Cobra, were selected to represent local Ferralsol and
1163 Acrisol. Twelve samples were sampled from CA and CO2.

1164
1165 **Fig. 3:** **A:** XRD pattern of CO2 samples, normalised to the maximal intensity of the 7.2A peak of the kaolinite. **B:**
1166 XRD pattern of the CA samples, normalised to the maximal intensity of the 4.95 peak of gibbsite. The CO2 55,
1167 CA 380, and CA 485 sample XRD has not been recorded due to the lack of sample. With: Kln : Kaolinite; Gbst:
1168 Gibbsite; Qtz: Quartz; Gte: Goethite; Hm: Hematite; Ant: Anatase (Ti Oxide); Chl: Chlorite; Sm: Smectite.

1169
1170 **Fig. 4:** **A:** EPR spectra of CO2 clay fractions. **B:** EPR spectra of CA clay fractions CA 280, 360 and 380 excluded
1171 due to their remaining magnetic minerals content influence in the $g=4$ zone. **C:** Zoom on the stretching zone
1172 of the CO2 clay fraction FTIR spectra. The spectra are normalized considering the 3620cm^{-1} band attributed to the
1173 kaolinite. The CO2 55 sample spectrum has not been recorded due to the lack of sample. **D:** Zoom on the stretching
1174 zone of the CA clay fraction FTIR spectra, CA 360 and 380 excluded due to the number of samples. The spectra
1175 are normalised considering the 3526cm^{-1} band attributed to gibbsite.

1176
1177 **Fig. 5:** **A:** Zoom of the $g=2$ zone of the CO2 clay fraction EPR spectra. **B:** Zoom of the $g=2$ zone of the CA clay
1178 fraction EPR spectra. With TIs: the $g = 2.006$ normalized intensity of the considered sample and TI_{dim} : the $g=2.007$
1179 normalized intensity of the dimex EPR signal, I_{zdim} : the normalized intensity of the 1.881 g signal of the EPR
1180 dimex spectra and I_{zs} : the normalized intensity of the 1.881 signal of the sample EPR spectra

1181
1182 **Fig. 6:** **A:** EPR spectra in the $g=2$ zone for irradiated CA samples, corresponding dosimetry curves and resulting
1183 paleodoses with a: CA 84, b: CA 200, c: CA 440, d: CA 480. The 10^{12} irradiation amplitude has not been
1184 considered as it appears aberrant. **B:** EPR spectra in the $g=2$ zone for irradiated CO2 samples, corresponding
1185 dosimetry curves and resulting paleodoses with samples. With a: CO2 45, b: CO2 200, c: CO2 280, d: CO2 450).

1186
1187 **Fig. 7** **A:** U and Th comparison for both parts of the two studied profiles with sa: Saprolite (C horizon) and ss: soil
1188 *solum*. **B:** Dose rate trend with depth of both profiles. The dash line is the soil *solum* and saprolite depth transition,
1189 with red square the Cajou (CA) sample (Ferralsol) and with black points the Cobra (CO2) samples (Acrisol).

1190
1191 **Fig. 8:** Kaolinites ages distribution over the Caju-Cobra transect.

1192
1193 **Fig.9:** Paleodose vs Dose rate plot of the studied samples, the open symbols are corresponding to the samples with
1194 an estimated paleodose. Three preferential periods of weathering can be identified: a Miocene-Pliocene period (6-
1195 3.6 Ma), a Pleistocene period (2.5-1.5 Ma) and a Quaternary period (1 Ma to Actual).

1196
1197 **Fig.10:** Updated schematic geomorphologic model of Curicuriari soil landform dynamic based on the local acrisol
1198 and ferralsol chronology.

1199
1200

1201 Tables captions:

1202

1203 **Table 1:** CA and CO2 horizon description and samples location. The samples noted with an * are the one used for
1204 artificial irradiation and have been investigated using fission tracks mapping methodology.

1205

1206 **Table 2:** Data table for the Caju (CA) profile and resulting calculated ages. The non-bold values are estimated
1207 ages.

1208

1209 **Table 3:** Data table for the Cobra (CO2) profile and resulting calculated ages. The non-bold values are estimated
1210 ages.

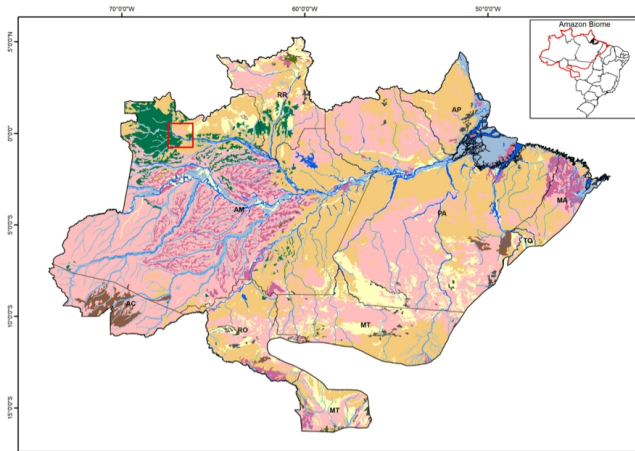
1211

1212 **Table 4:** Data table of the ^{238}U , ^{222}Rn , ^{226}Ra and ^{232}Th activity obtained by gamma spectroscopy. Ratio between
1213 the two activity have been performed to assess the equilibrium of the decay chain.

1214

1215

A



LEGEND

- Water bodies
- Drainage network

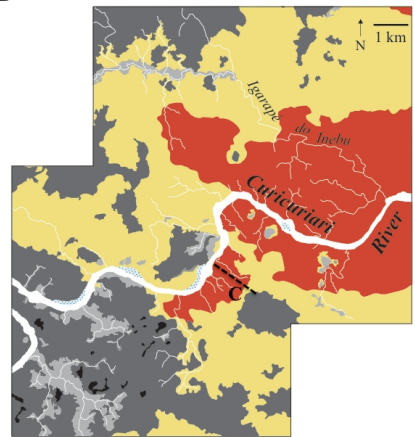
Soil Types (FAO, 1998)

- | | | |
|------------|-------------|--------------------------|
| Cambisols | Plinthosols | Arenosols |
| Gleysols | Podzols | Planosols |
| Ferralsols | Acrisols | Studied Curicuriari area |
| Leptsols | Vertisols | |

Cartographic Informations
 Digital cartographic base scale: 1:1 000 000, obtained from cartographic digital integrated database of Brazil to the millionth from IBGE
 Geographic Projection
 Datum WGS1984
 Edition and organization: José Roberto A. Mantovanini (October 2017)
 Guilherme Taitson Bueno
 Adapted from MMA (Pedological map)



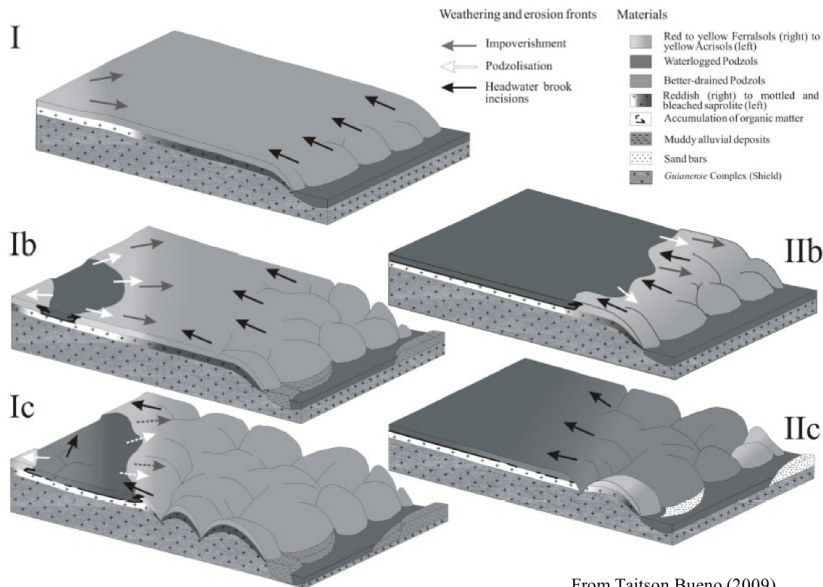
B



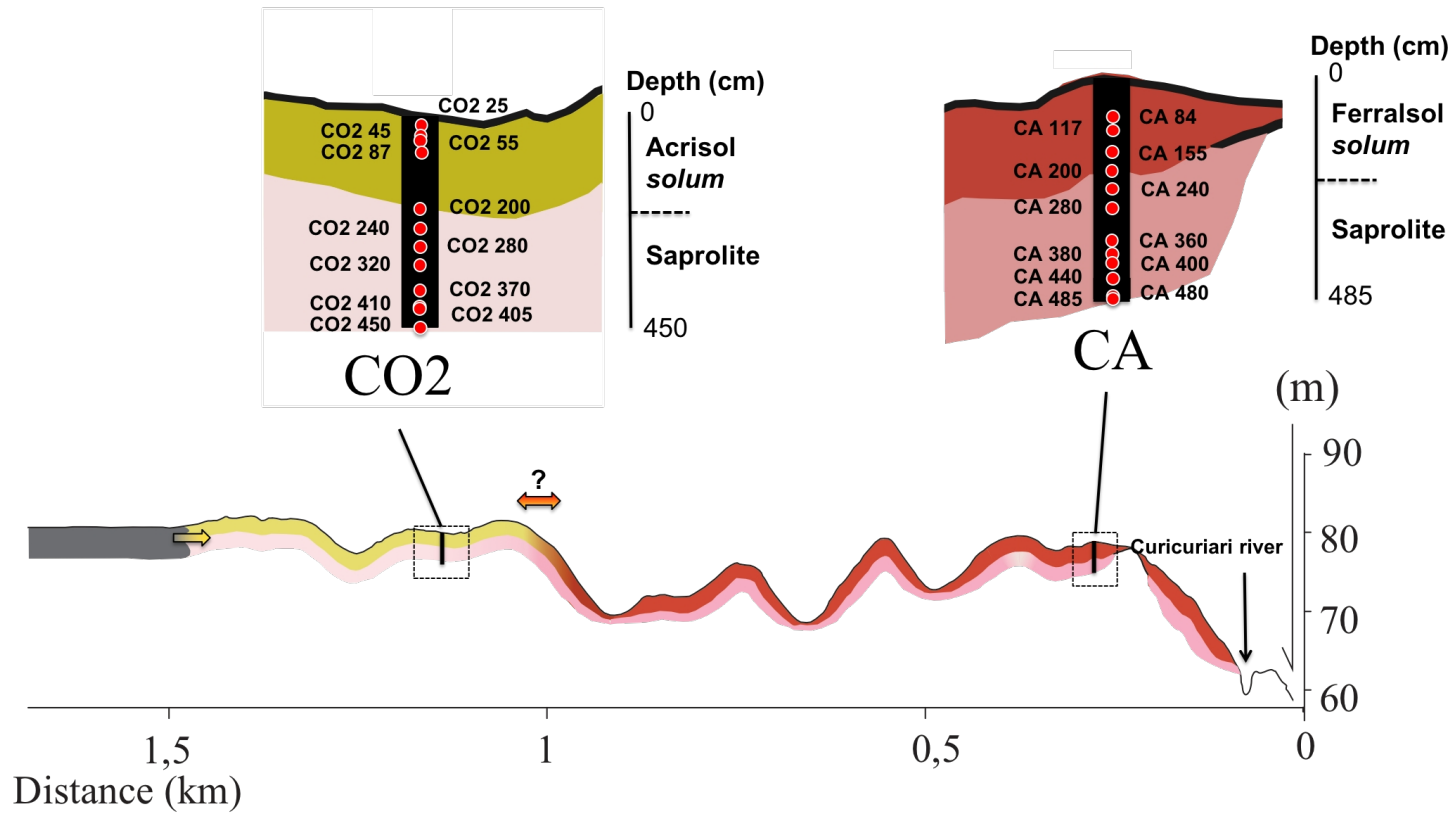
Cajou-Cobra transect

- White sand bars and rock outcrops
- Incised plateau edges, with red to yellow Ferralsols (forest)
- Slightly incised plateaux with yellow Acrisols (forest)
- Inundated plain and depressions with seasonally waterlogged Podzols (*Campinarana*)
- Depression centres with overflowed Podzols (*Campina*)
- Incised plain with better-drained Podzols, (*Caatinga* and riparian forest)
- Bleached saprolite
- Reddish saprolite

C

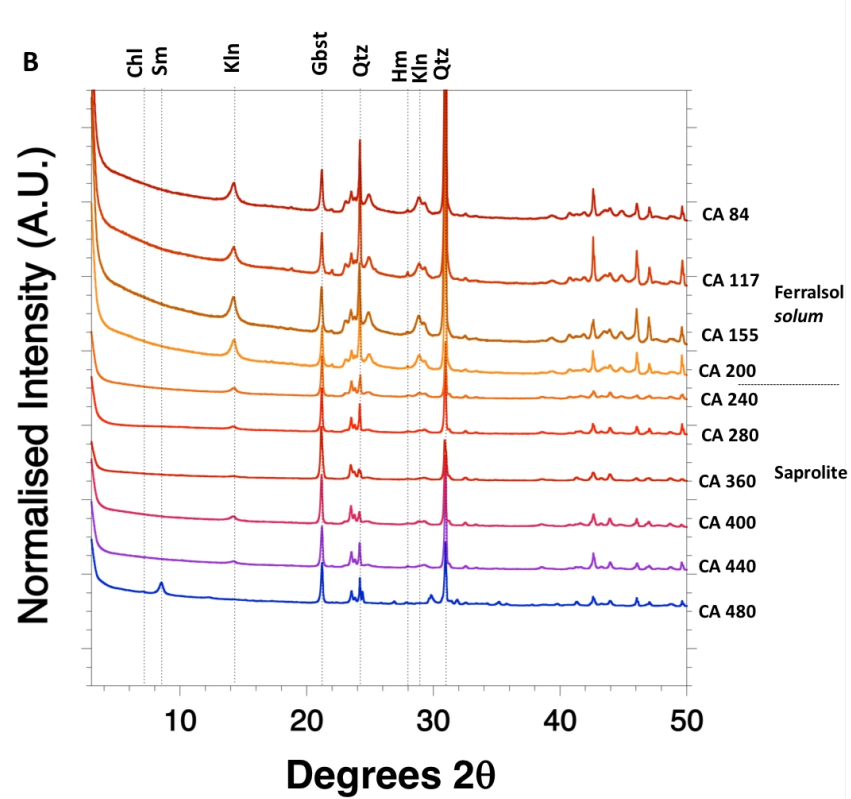
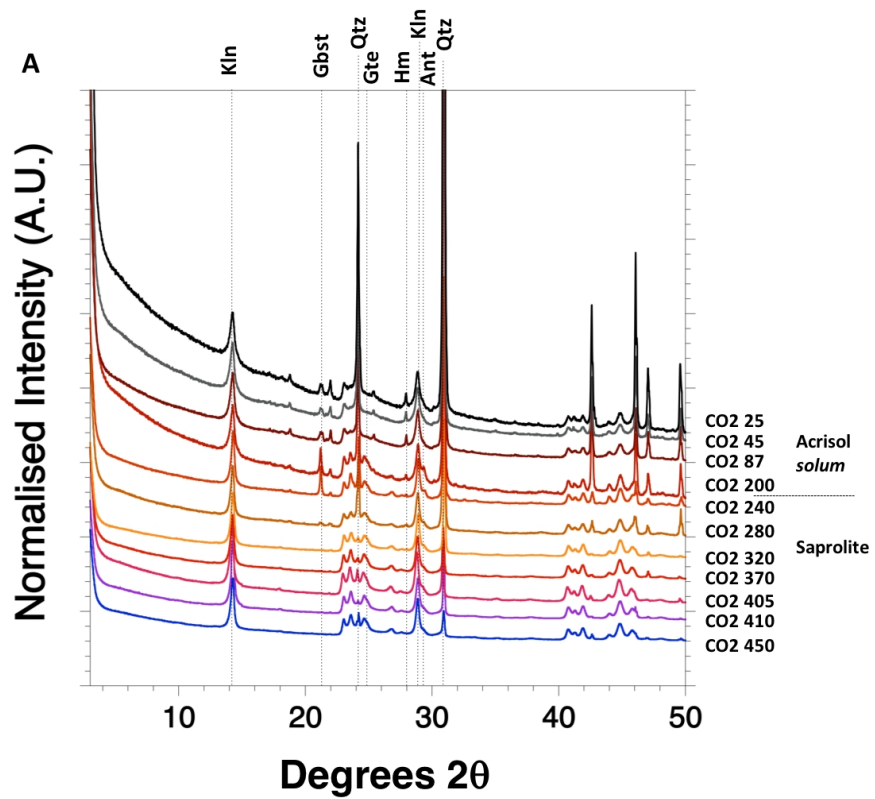


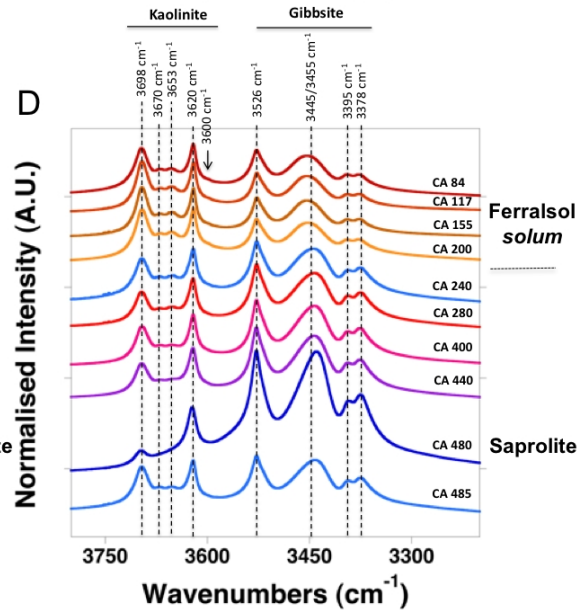
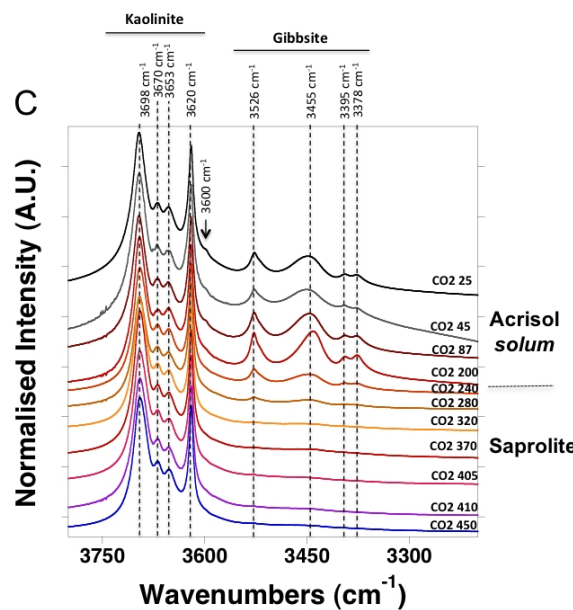
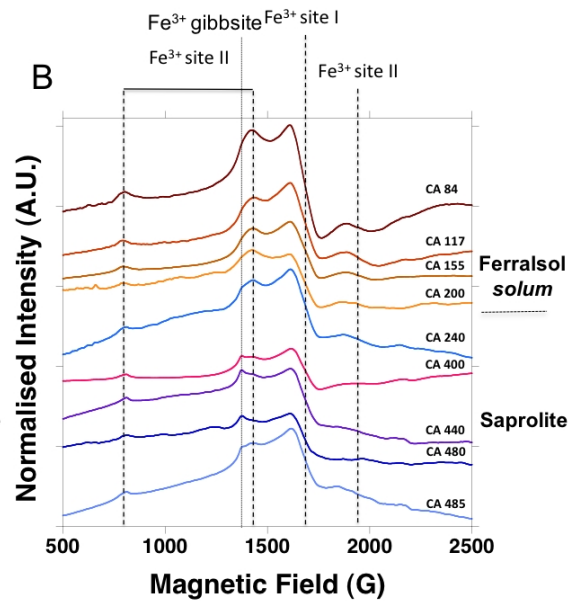
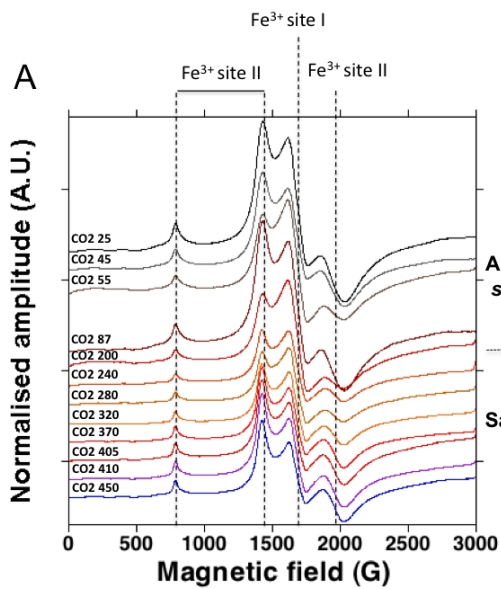
From Taitson Bueno (2009)

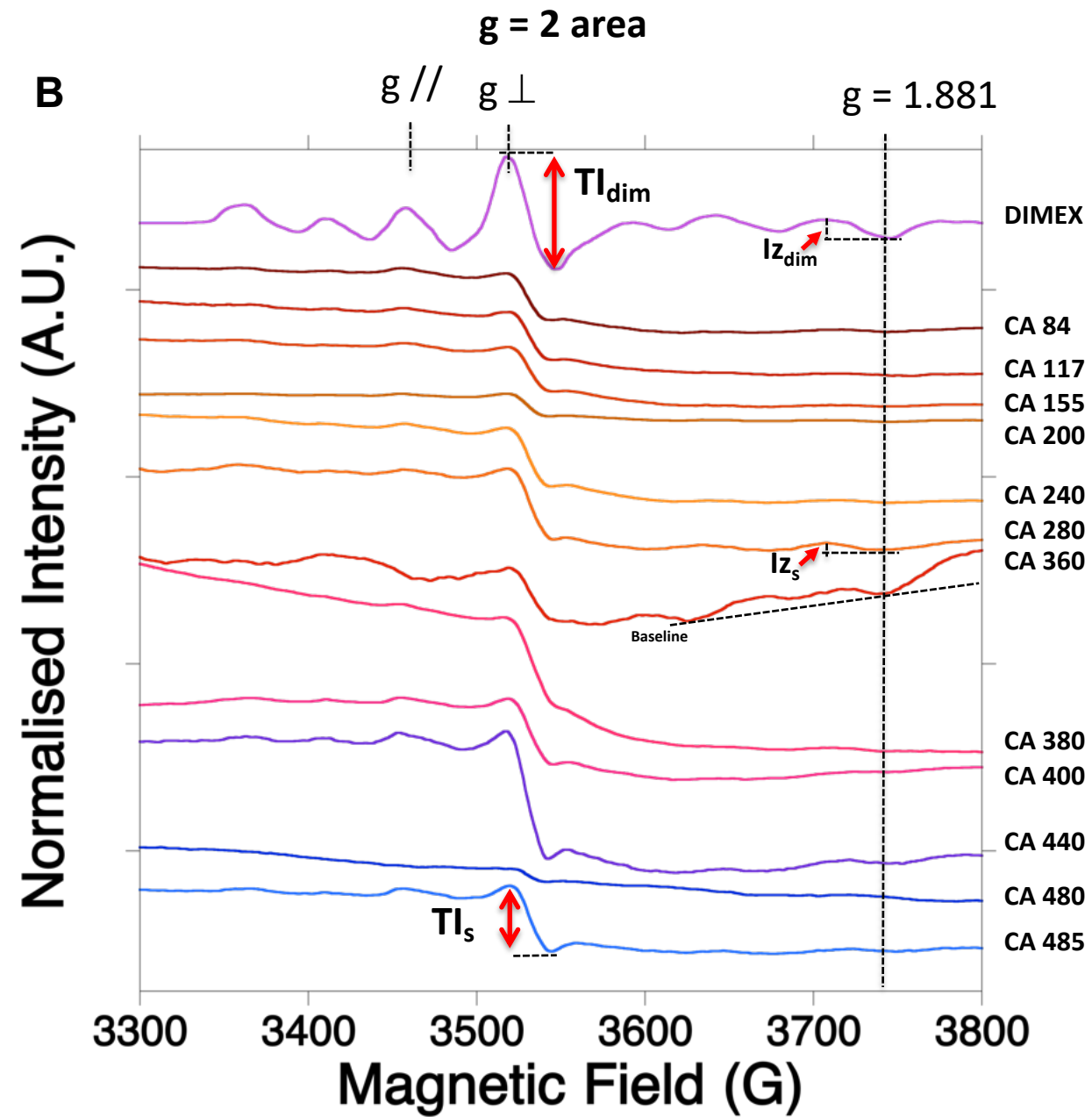
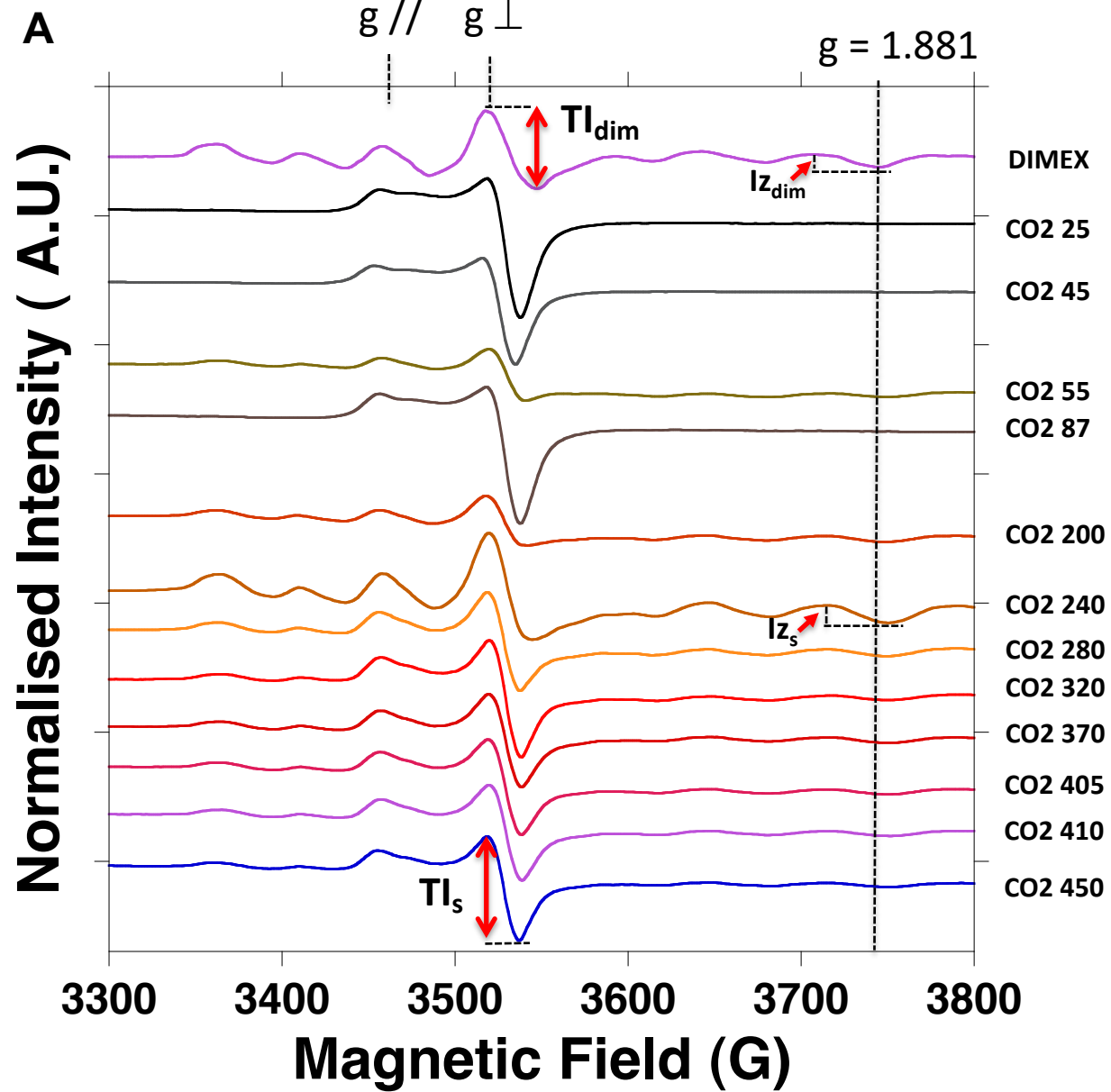


- Incised plateau edges, with red to yellow Ferralsols (forest)
- Slightly incised plateaux with yellow Acrisols (forest)
- Inundated plain and depressions with seasonally waterlogged Podzols (*Campinarana*)

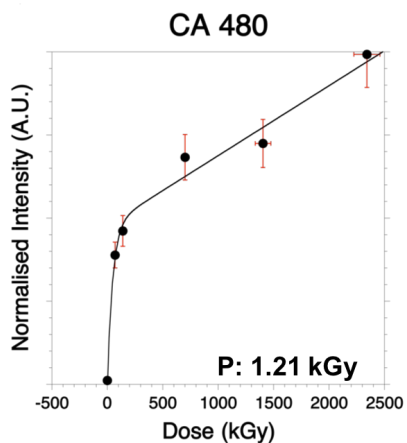
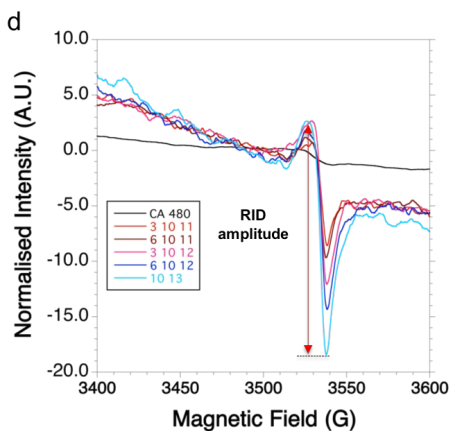
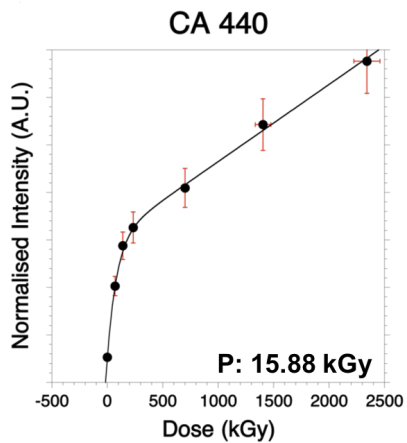
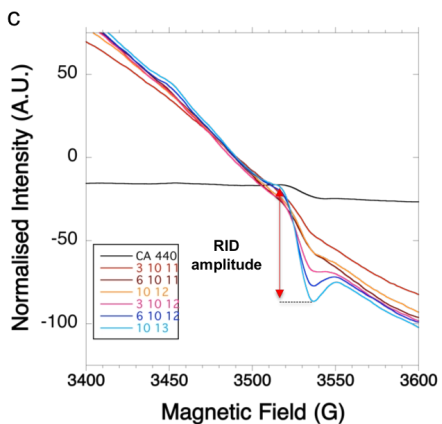
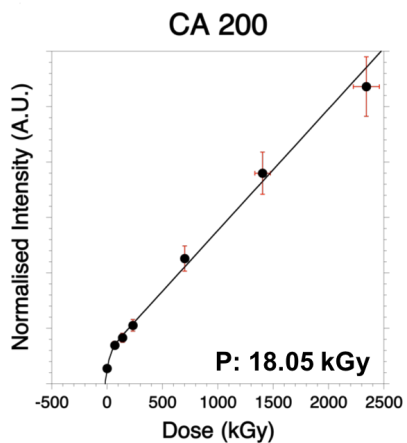
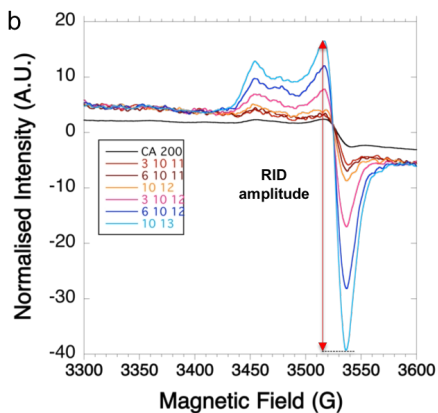
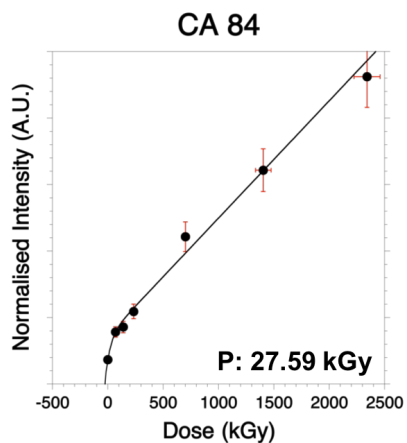
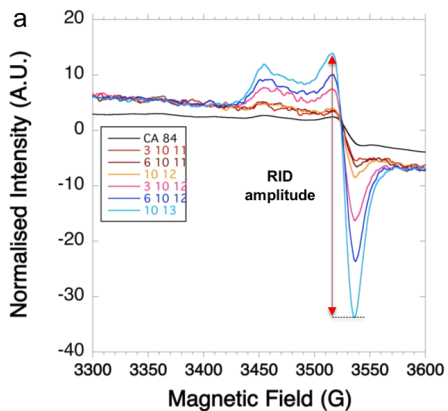
- Bleached saprolite
- Reddish saprolite

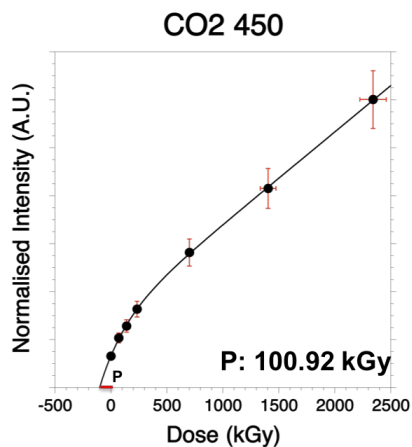
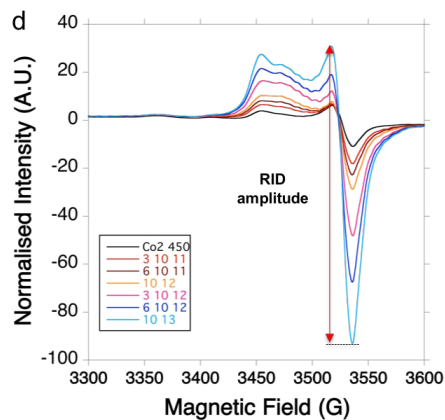
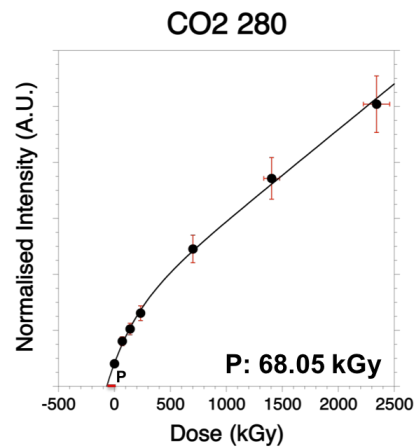
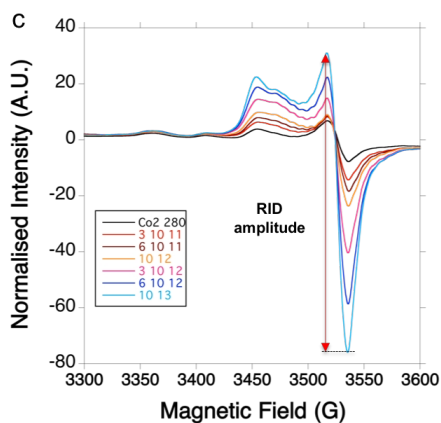
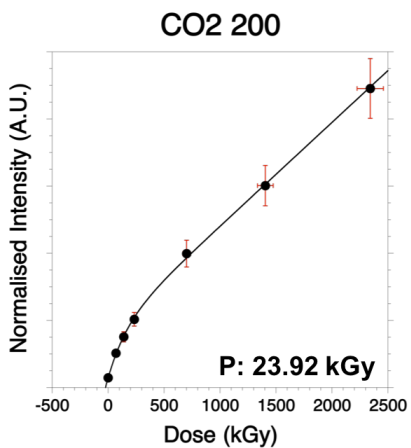
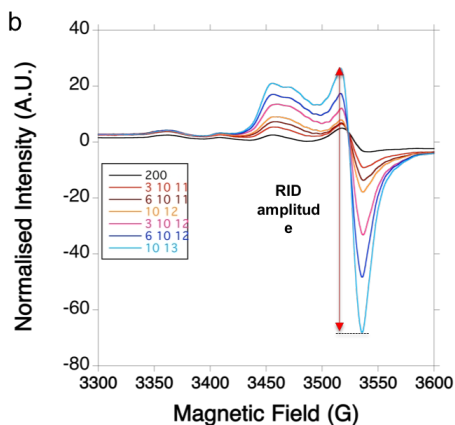
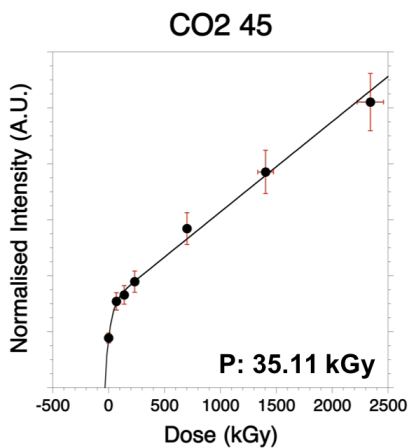
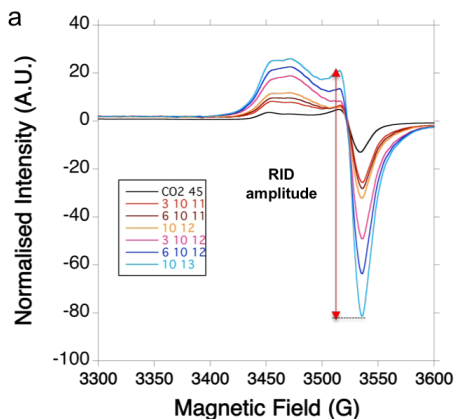


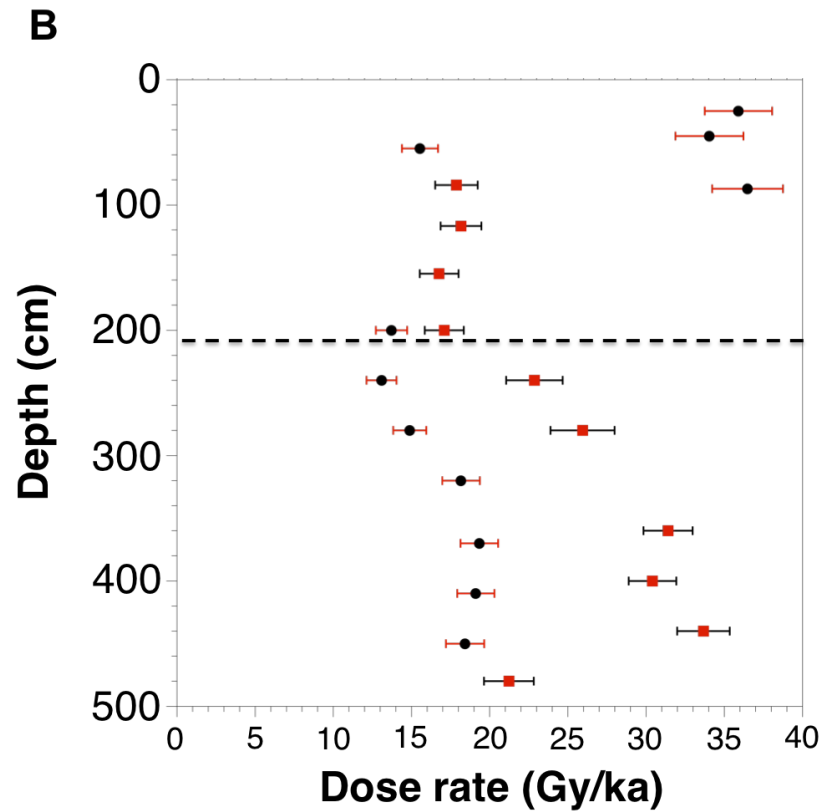
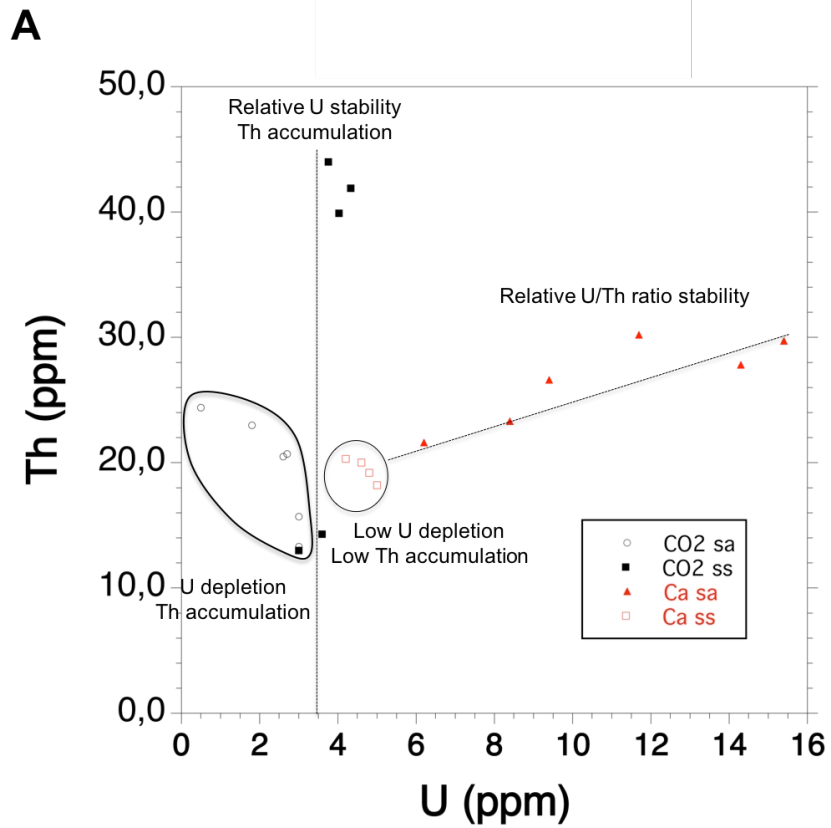


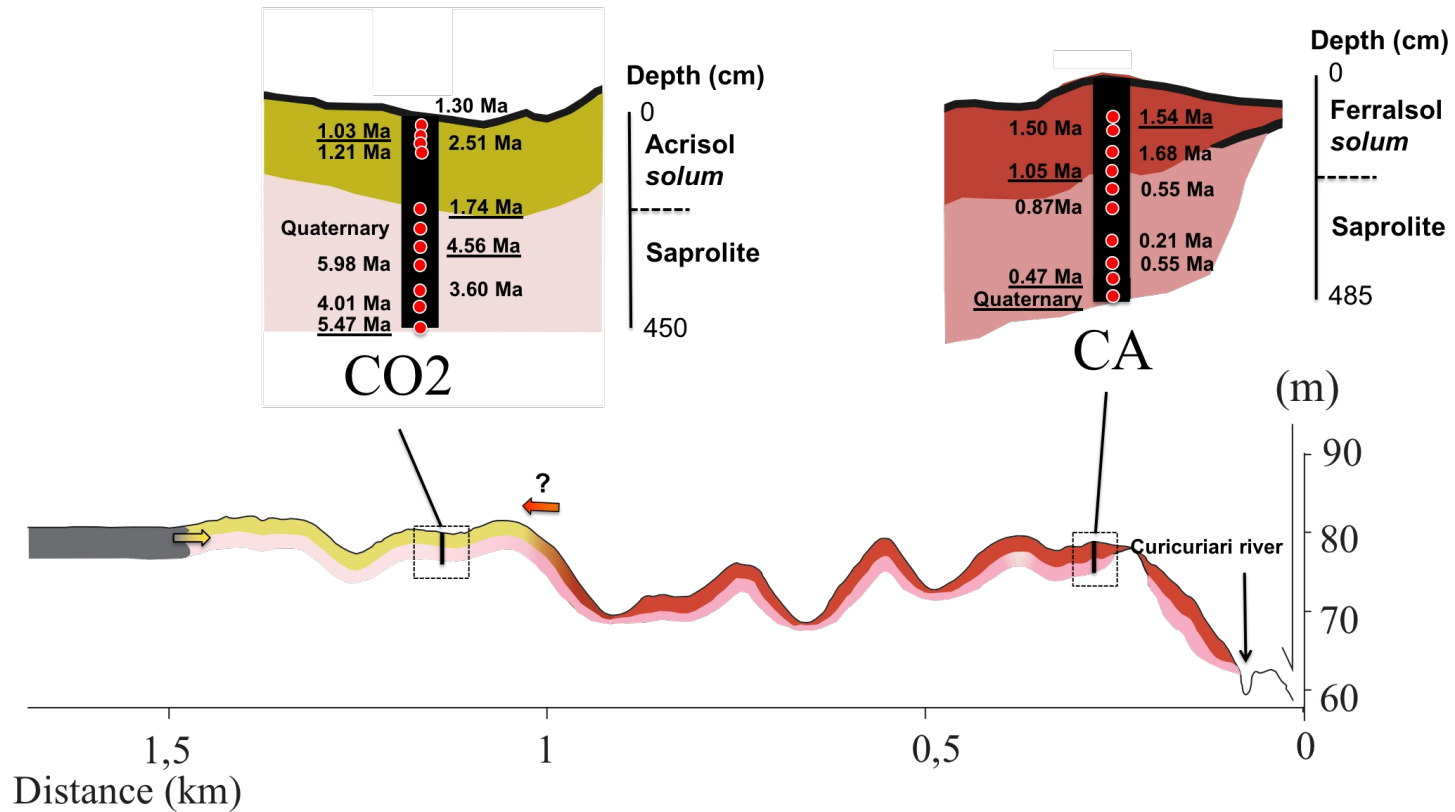


A

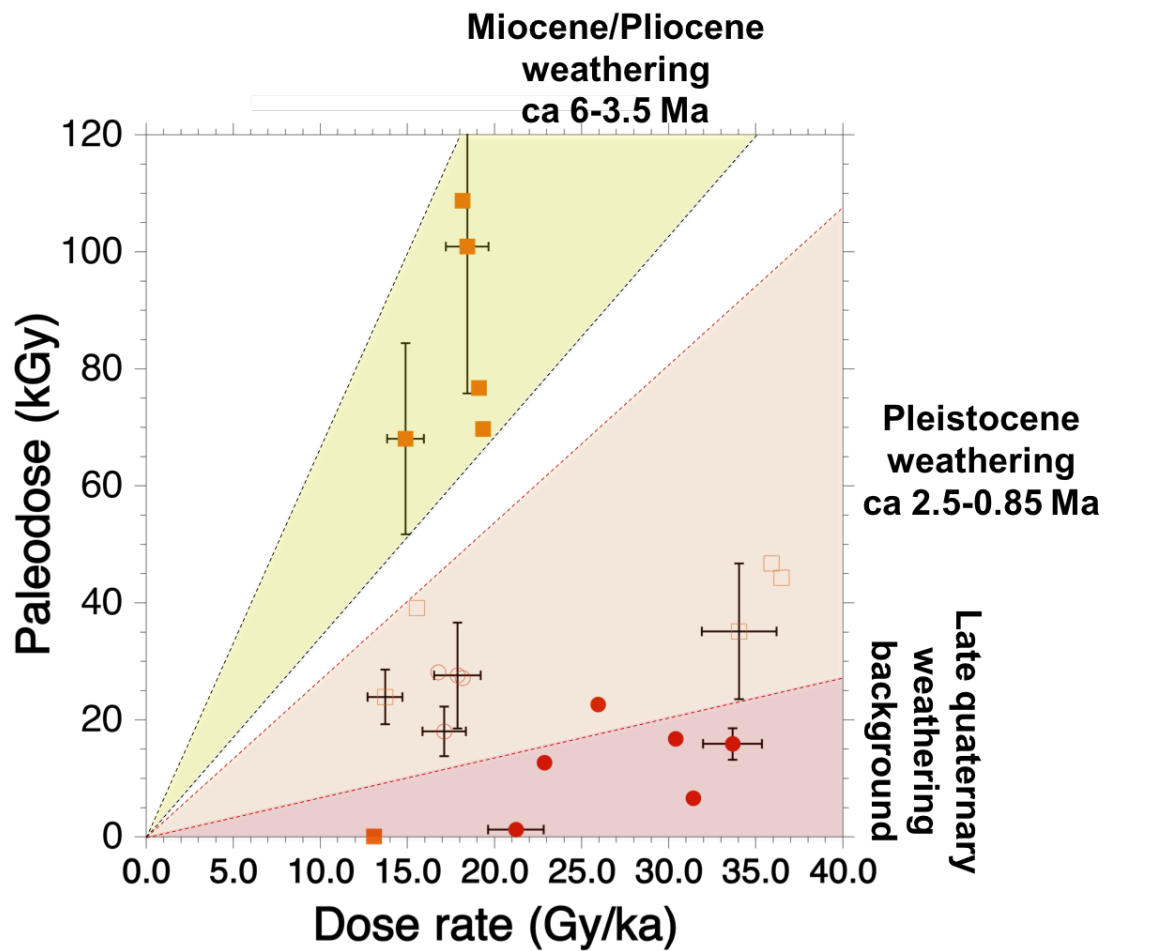


B





- Incised plateau edges, with red to yellow Ferralsols (forest)
- Slightly incised plateaux with yellow Acrisols (forest)
- Inundated plain and depressions with seasonally waterlogged Podzols (*Campinarana*)
- Bleached saprolite
- Reddish saprolite



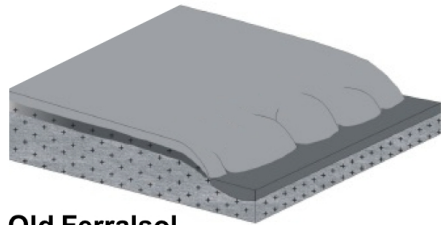
□ Acrisol (CO₂) solum samples

○ Ferralsol (CA) solum samples

■ Acrisol (CO₂) saprolite samples

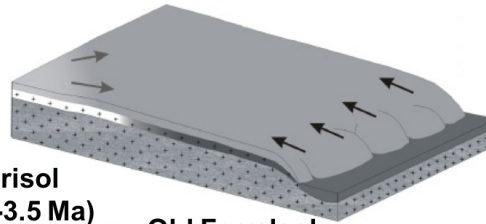
● Ferralsol (CA) saprolite samples

I. Formation of an initial Ferralsol (>6 Ma)



Old Ferralsol (>6 Ma)

II. Late Miocene/Pleistocene weathering: Impoverishment of the Ferralsol and its progressive total transformation into a younger Acrisol

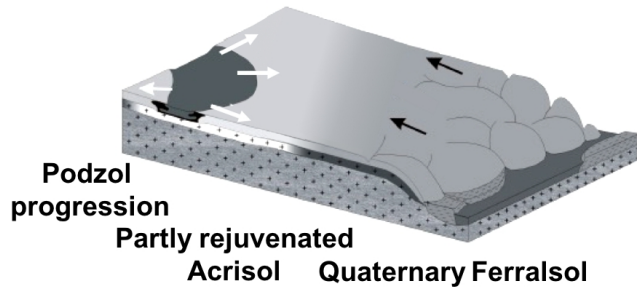


Acrisol (ca 6-3.5 Ma)

Old Ferralsol (>6 Ma)

III. Quaternary incision and weathering reactivation: A quaternary Ferralsol formed in parallel to the plateau incision

IV. Futur of the Curicuriari catchment ?



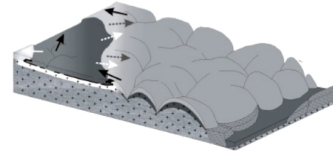
Podzol progression

Partly rejuvenated

Acrisol

Quaternary Ferralsol

Incision faster than podzolization



Podzolization faster than incision



Materials

- Red to yellow Ferralsols (right) to yellow Acrisols (left)
- Waterlogged Podzols
- Better-drained Podzols
- Reddish (right) to mottled and bleached saprolite (left)
- Accumulation of organic matter
- Muddy alluvial deposits
- Sand bars
- Guianense Complex (Shield)

Weathering and erosion fronts

- Impoverishment
- Podzolisation
- Headwater brook incisions

CA	Depth (cm)	Profile section	Color	Texture	Structure	Porosity	Samples
A11	0-22	Ferrasol	Dark brown (7.5YR 3/4)	Sandy clay loam with coarse sand	Granular	Highly porous	/
A12	22-41	Ferrasol	Strong brown (7.5YR 4/6)	Sandy clays with fine and coarse sand	Granular to blocky	Porous	/
B(r)	41-205	Ferrasol	Brown (5YR 5/8)	Sandy clay with fine and coarse sand	Blocky with numerous micropeds	Porous	CA 84* CA 117 CA 155 CA 200*
BC(r)	205-345	Saprolite	Red (2.5YR to 10R 4/6)	Sandy clay loam with coarse sands	Massive to blocky with micropeds	Porous	CA 240 CA 280
BC(r)	345-475	Saprolite	Red (10 R 4/6)	Sandy clay loam with coarse sands	Massive	Porous	CA 360 CA 380 CA 400 CA 440*
C3	475- ?	Saprolite	Heterogeneous	Weathered rock horizon with numerous relics of feldspatic and mafic minerals with small amount of clay	/	No porosity	CA 480* CA 485

CO2	Depth (cm)	Profile section	Color	Texture	Structure	Porosity	Samples
A11	0-15	Acrisol	Olive brown (2.5YR 4/3)	Loamy sand with coarse	Granular	Porous	/
A12	15-42	Acrisol	Light olive brown (2.5YR 5/4)	Sandy loam with fine to coarse sands	Blocky to massive	Weakly porous	CO2 25
B(y)	42-126	Acrisol	Yellowish brown (10YR 6/6)	Sandy clay loam with fine and coarse sand	Blocky to massive	Porous	CO2 45* CO2 55 CO2 87
B(r)	126-215	Acrisol	Reddish yellowish (7.5YR 6/6)	Sandy clay loam with fine and coarse sand	Blocky with micropeds	Porous	CO2 200*
BCg (r-y)	215-365	Saprolite	Mottled: Reddish yellow (2.5-5 YR 6/6) Bownish yellow (10YR 6/8) White	Sandy clay loam with fine and coarse sands	Massive	No porosity	CO2 240 CO2 280* CO2 320
BCg (w-y)	365-455	Saprolite	Mottled: White Brownish yellow (1YR 6/8) Reddish yellow (2.5-5YR 6/6)	Sandy clay loam with fine and coarse sands Weathered primary minerals can be observed	Massive	No porosity	CO2 370 CO2 405 CO2 410 CO2 450*

Name	Group	Center-A Content (A.U.)	U (ppm)	Th (ppm)	K (%)	% U matrice	DR (Gy/ka)	DR corrected (Gy/ka)	Paleodose (kGy)	Age (Ma)
CA 84	CA1	3.67	5	18.2	0.0664	48.26	29.95	17.88	27.59_{+/-8.8}	1.54_{+/-0.50}
CA 117	CA1	3.63	4.2	20.3	0.0332	48.26	29.18	18.18	27.19	1.50
CA 155	CA1	3.73	4.8	19.2	0.0083	34.42	30.09	16.77	28.17	1.68
CA 200	CA2	2.76	4.6	20	0.0332	34.42	30.15	17.10	18.05_{+/-4.03}	1.05_{+/-0.25}
CA 240	CA1	1.94	8.4	23.3	0.0581	34.42	44.39	22.87	12.69	0.55
CA 280	CA1	3.15	9.4	26.6	0.0913	34.42	50.12	25.94	22.64	0.87
CA 360	CA3	2.33	14.3	27.8	0.0913	34.42	65.98	31.41	6.63	0.21
CA 380	CA 3	7.50	NA	NA	NA	34.42	NA	NA	17.13	NA
CA 400	CA3	5.58	11.7	30.2	0.0664	34.42	59.99	30.41	16.77	0.55
CA 440	CA3	5.31	15.4	29.7	0.0996	34.42	70.87	33.67	15.88_{+/-2.56}	0.47_{+/-0.08}
CA 480	CA4	0.24	6.2	21.6	1.9173	34.42	38.24	21.23	1.21_{+/-0.17}	Quaternary
CA 485	CA 1	5.31	NA	NA	NA	34.42	NA	NA	11.8	NA

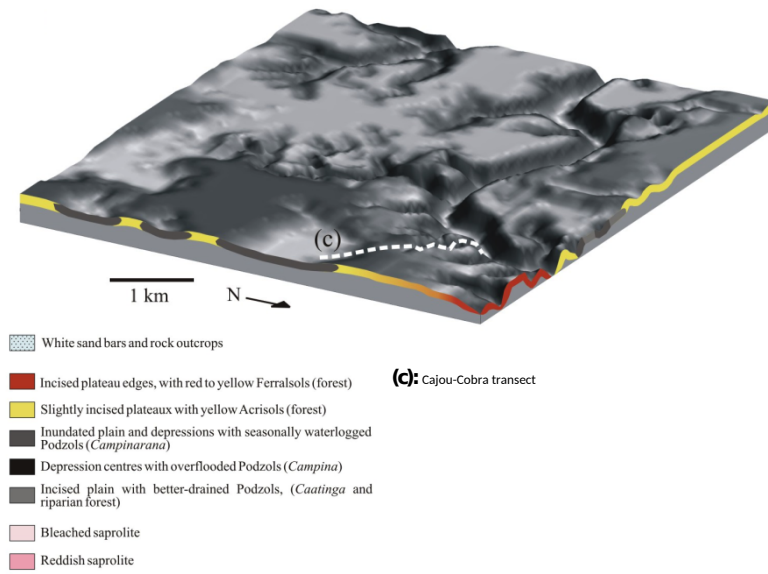
Name	Group	Center-A Content (A.U.)	U (ppm)	Th (ppm)	K (%)	% U matrice	DR (Gy/ka)	DR corrected (Gy/ka)	Paleodose (kGy)	Age (Ma)
CO2 25	C1	21.23	4.3	41.65	0	55.8	46.97	35.91	46.736	1.302
CO2 45	C1	17.76	4.03	39.9	0	55.8	44.44	34.05	35.11_{+/-11.34}	1.031_{+/-0.34}
CO2 55	C2	4.64	3.6	14.3	0.0083	55.8	22.49	15.55	39.12	2.515
CO2 87	C1	20.57	3.76	44	0	55.8	46.93	36.49	44.28	1.213
CO2 200	C2	2.92	3	13	0.0166	55.8	19.62	13.72	23.92_{+/-4,33}	1.743_{+/-0.34}
CO2 240	C3	0	3	13.3	0.0415	28.83	19.89	13.09	Negligible	Quaternary
CO2 280	C3	8.11	3	15.7	0.0083	28.83	21.79	14.90	68.05_{+/-15,99}	4.568_{+/-1.12}
CO2 320	C4	14.05	2.6	20.5	0.0166	28.83	24.46	18.18	108.73	5.982
CO2 370	C4	9.55	1.8	23	0.0664	28.83	24.1	19.35	69.74	3.605
CO2 405	C4	10.42	NA	NA	NA	28.83	NA	NA	76.95	NA
CO2 410	C4	10.4	0.5	24.4	0.0332	28.83	21.24	19.12	76.735	4.013
CO2 450	C4	13.13	2.7	20.7	0.0332	28.83	24.94	18.44	100.92_{+/-24,2}	5.473_{+/-1.36}

Sample	^{238}U dpm/g	^{222}Rn dpm/g	Rn/U	^{226}Ra dpm/g	^{232}Th dpm/g
CA84	4.05+/-0.13	4.0104+/-0.04	0.989	4.6266+/-0.26	6.6782+/-0.084
CO2 200	2.379+/-0.08	2.791+/-0.028	1.173	2.87535+/-0.158	4.2054+/-0.028
CO2 450	1.904+/-0.10	2.606+/-0.035	1.368	2.905+/-0.2	7.2946+/-0.075

Declaration of competing interest

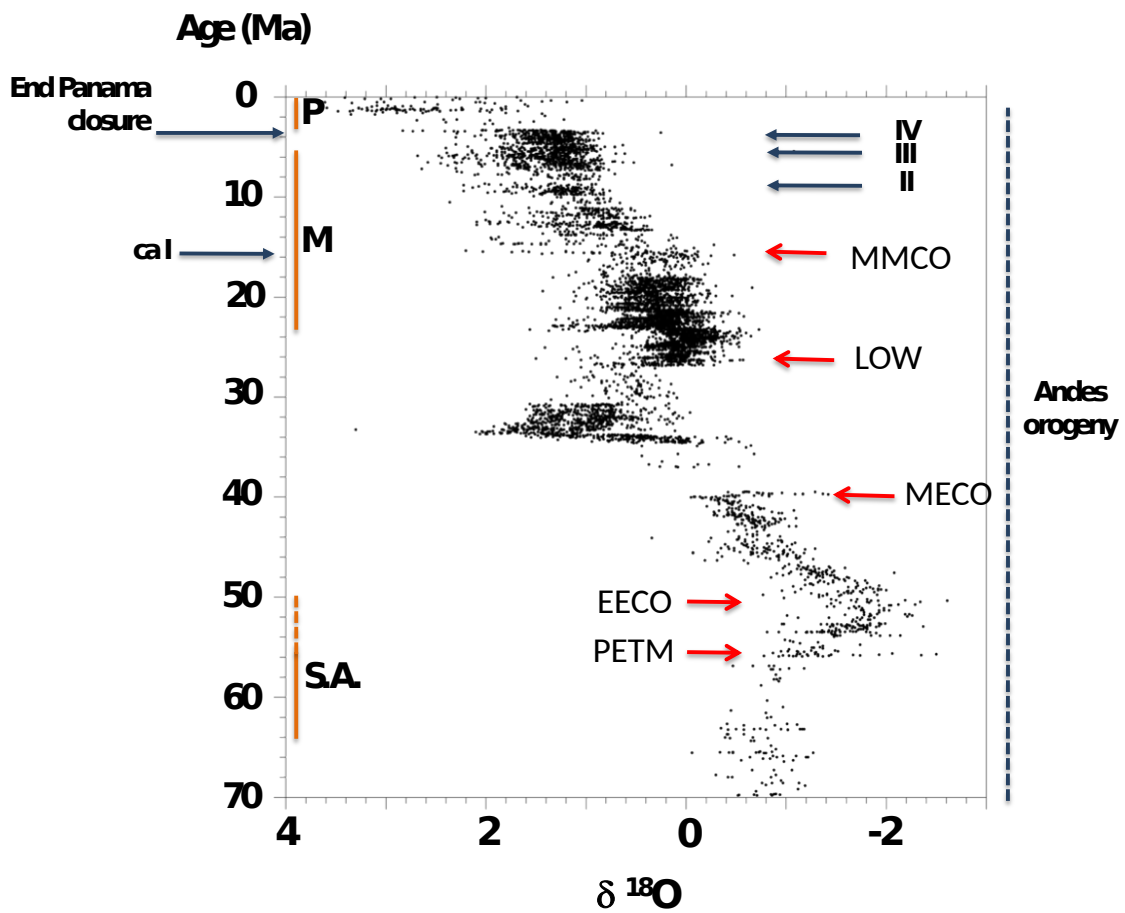
The authors declare that they have no known competing financial interests or personal relationships that could have appeared to influence the work reported in this paper.

SI 1:



SI 1: Topography and soils repartition of the Curicuriari basin studied area with (c) the Cajou-Cobra transects.

SI 2:



SI2: Delta ^{18}O curve from all oceans from Cramer (2009), the main warming peak and geodynamics events that have affected Amazonia are reported. With: PETM: Paleocene/Eocene Temperature Maximum, EECO: Early Eocène Climatic Optimum, MECO: Mid Eocene Climatic Optimum, LOW: Late Oligocene Warming, MMCO: Mid Miocène Climatic Optimum. The major late tertiary phases of Andean uplifts are reported as ca I: Quechua I; II: Quechua II, III: Quechua III and IV: Pliocene uplift.

SI 3:

A

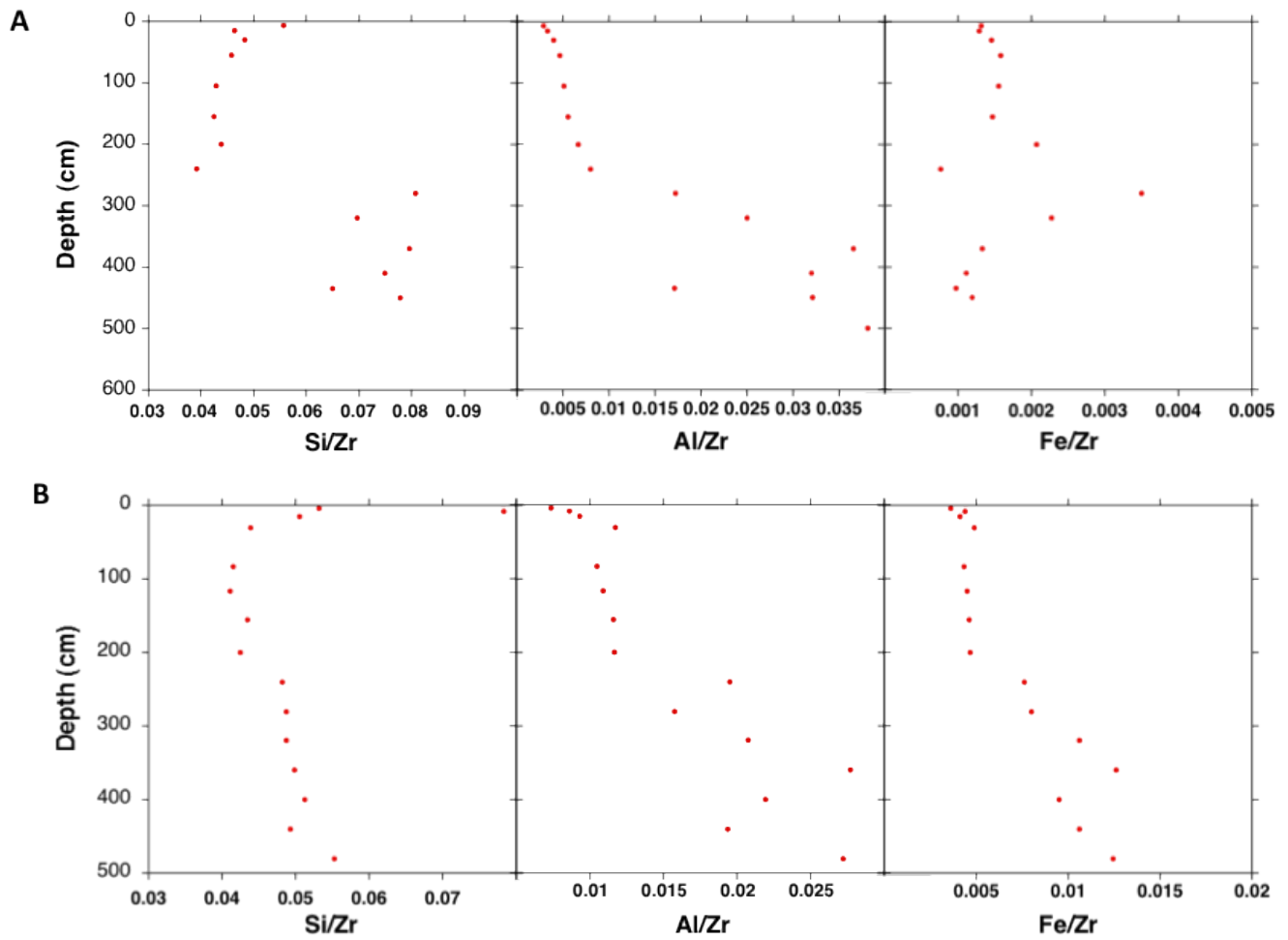
Name	SiO₂ (%)	Al₂O₃ (%)	Fe₂O₃ (%)	TiO₂ (%)	Zr (ppm)	Si/Zr	Al/Zr	Fe/Zr
CA 4	68.92	9.58	4.72	1.105	1297	0.0531	0.0074	0.0036
CA 8	78.8	8.7	4.39	1.015	1006	0.0783	0.0086	0.0044
CA 15	70.4	12.91	5.69	1.491	1392	0.0506	0.0093	0.0041
CA 30	62.86	16.82	6.99	1.869	1431	0.0439	0.0118	0.0049
CA 84	64.5	16.29	6.76	1.832	1554	0.0415	0.0105	0.0044
CA 117	64.28	17.03	7.03	1.913	1562	0.0412	0.0109	0.0045
CA 155	64.25	17.13	6.83	1.905	1477	0.0435	0.0116	0.0046
CA 200	63.74	17.5	7.03	1.94	1499	0.0425	0.0117	0.0047
CA 240	54.62	22.06	8.65	2.061	1132	0.0483	0.0195	0.0076
CA 280	58.06	18.74	9.54	2.261	1191	0.0487	0.0157	0.0080
CA 320	51.19	21.82	11.18	2.258	1051	0.0487	0.0208	0.0106
CA 360	45.08	25.07	11.4	2.09	904	0.0499	0.0277	0.0126
CA 400	52.01	22.33	9.66	2.329	1016	0.0512	0.0220	0.0095
CA 440	53.15	20.9	11.44	2.393	1078	0.0493	0.0194	0.0106
CA 480	46.53	22.9	10.46	1.798	842	0.0553	0.0272	0.0124

B:

Name	SiO₂ (%)	Al₂O₃ (%)	Fe₂O₃ (%)	TiO₂ (%)	Zr (ppm)	Si/Zr	Al/Zr	Fe/Zr
CO 2-7	84.92	4.46	2.02	1.011	1527	0.0556	0.0029	0.0013
CO 2-15	82.86	5.93	2.31	1.296	1790	0.0463	0.0033	0.0013
CO 2-30	82.82	6.83	2.51	1.404	1717	0.0482	0.0040	0.0015
CO 2-55	81.34	8.33	2.82	1.582	1775	0.0458	0.0047	0.0016
CO 2-105	80.37	9.62	2.93	1.719	1878	0.0428	0.0051	0.0016
CO 2-155	79.72	10.37	2.78	1.641	1882	0.0424	0.0055	0.0015
CO 2-200	77.05	11.66	3.63	1.478	1756	0.0439	0.0066	0.0021
CO 2-240	74.81	15.24	1.47	1.257	1907	0.0392	0.0080	0.0008
CO 2-280	72.2	15.41	3.13	1.233	895	0.0807	0.0172	0.0035
CO 2-320	63.15	22.71	2.07	1.676	907	0.0696	0.0250	0.0023
CO 2-370	58.69	26.99	0.98	1.838	738	0.0795	0.0366	0.0013
CO 2-410	60.41	25.82	0.9	1.797	806	0.0750	0.0320	0.0011
CO 2-435	69.97	18.4	1.04	2.473	1076	0.0650	0.0171	0.0010
CO 2-450	61.36	25.32	0.94	1.769	789	0.0778	0.0321	0.0012

SI 3: Tables representing the SiO₂, Al₂O₃, Fe₂O₃, TiO₂ and Zr content and Si/Zr, Al/Zr and Fe/Zr calculations for CA (A), CO2 (B).

SI 4:



SI 4: Si, Al and Fe content compared to Zr content evolution within Ca (A) and CO2 (B).

SI 5:

Sample	Ratio I Kln/I Gbst	Ratio I Kln/I Qtz
<i>CO2 450</i>	98,1	3,4
<i>CO2 410</i>	164,8	2,8
<i>CO2 405</i>	164,9	1,8
<i>CO2 370</i>	136,6	2,1
<i>CO2 320</i>	62,6	0,8
<i>CO2 280</i>	17,7	0,3
<i>CO2 240</i>	3,4	0,5
<i>CO2 200</i>	3,0	0,2
<i>CO2 87</i>	6,7	0,1
<i>CO2 45</i>	7,5	0,1
<i>CO2 25</i>	6,3	0,1

Sample	Ratio I Gbst/I Kln	Ratio I Gbst/I Qtz
<i>CA 480</i>	20,2	0,7
<i>CA 440</i>	7,3	0,5
<i>CA 400</i>	5,0	0,8
<i>CA 360</i>	20,0	1,5
<i>CA 280</i>	4,7	0,5
<i>CA 240</i>	4,0	0,9
<i>CA 200</i>	1,2	0,2
<i>CA 155</i>	1,5	0,2
<i>CA 117</i>	1,9	0,1
<i>CA 84</i>	1,4	0,2

SI 5: Ratios of Integrated area of the diagnostic peaks of 3 main minerals (Kaolinite (Kln); Quartz (Qtz); Gibbsite (Gbst)) observed with the XRD in the Acrisol (Cobra, CO2) and Ferralsol (Cajou, CA) profiles. Note that the present approach only provides a qualitative assesment of the variations of mineral proportions among the samples.

SI 6:

	Amplitude g=1.881	$R_{VO}^{2+} \times 100$	Amplitude g=2	$TI_{dim} \times R_{VO}^{2+}$	I_{RID}
<i>DIMEX</i>	1.9547	100	12.014	12.014	0
CO2 45	0.059	3.02	18.12	0.36	17.76
CO2 200	0.907	46.40	8.49	5.57	2.92
CO2 280	1.058	54.13	14.614	6.50	8.11
CO2 450	0.642	32.84	17.08	3.95	13.13
CO2 25	0.07	3.58	21.66	0.43	21.23
CO2 55	0.555	28.39	8.048	3.41	4.64
CO2 87	0.111	5.68	21.25	0.68	20.57
CO2 240	2.7	138.13	16.596	16.59	0.001
CO2 320	0.673	34.43	18.19	4.14	14.05
CO2 370	0.795	40.67	14.44	4.89	9.55
CO2 405	0.725	37.09	14.88	4.46	10.42
CO2 410	0.729	37.29	14.88	4.48	10.4
	Amplitude g=1.881	$R_{VO}^{2+} \times 100$	Amplitude g=2	$TI_{dim} \times R_{VO}^{2+}$	I_{RID}
<i>DIMEX</i>	1.9547	100	12.014	12.014	0
CA 84	0.25	12.79	5.21	1.54	3.67
CA 200	0.36	18.42	4.971	2.21	2.76
CA 440	0.496	25.37	8.36	3.05	5.31
CA 480	0.19	9.72	1.41	1.17	0.24
CA 117	0.24	12.02	5.075	1.447	3.63
CA 155	0.166	8.49	4.75	1.02	3.73
CA 240	0.71	36.32	6.3	4.36	1.94
CA 280	0.72	36.83	7.575	4.425	3.15
CA 360	0.92	47.06	7.988	5.65	2.33
CA 380	0.36	18.42	9.708	2.21	7.495
CA 400	0.237	12.12	7.0416	1.47	5.58
CA 485	0.281	14.375	7.0416	1.73	5.31

SI 6: Vanadium calculations parameters for CA and CO2. The presented intensities are in arbitrary units (A.U.).

SI 7:

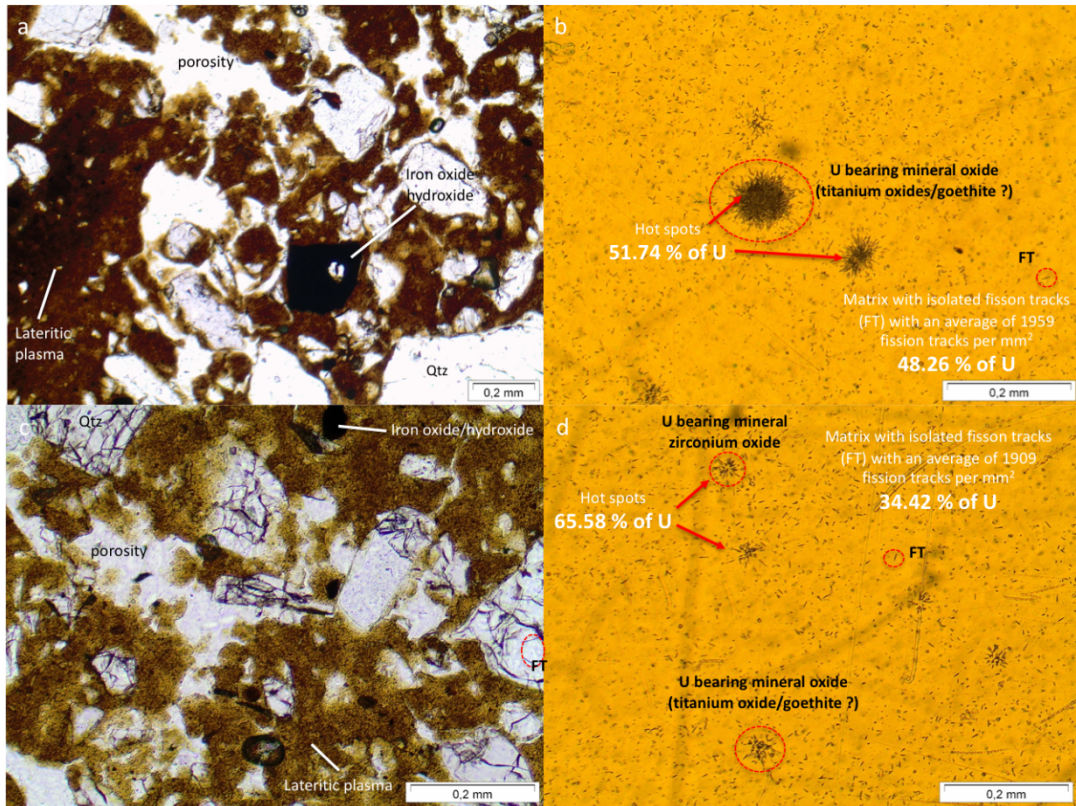
Nom	Group	I_{∞}	μ	P	FI
CA 84	CA1	6.82931	0.0227504	27.5937	0.0176381
CA 200	CA2	5.31906	0.0325731	18.0472	0.0219315
CA 440	CA3	29.9766	0.0116196	15.8807	0.0162449
CA 480	CA4	9.5483	0.020617	1.2083	0.0042056

Nom	Famille	I_{∞}	μ	P	FI
CO2 45	C1	29.3814	0.0237984	35.1125	0.032279
CO2 200	C2	16.4384	0.00597831	23.9165	0.0309003
CO2 280	C3	24.2533	0.00417967	68.0466	0.0326472
CO2 450	C4	25.52039	0.004489324	100.9248	0.03859895

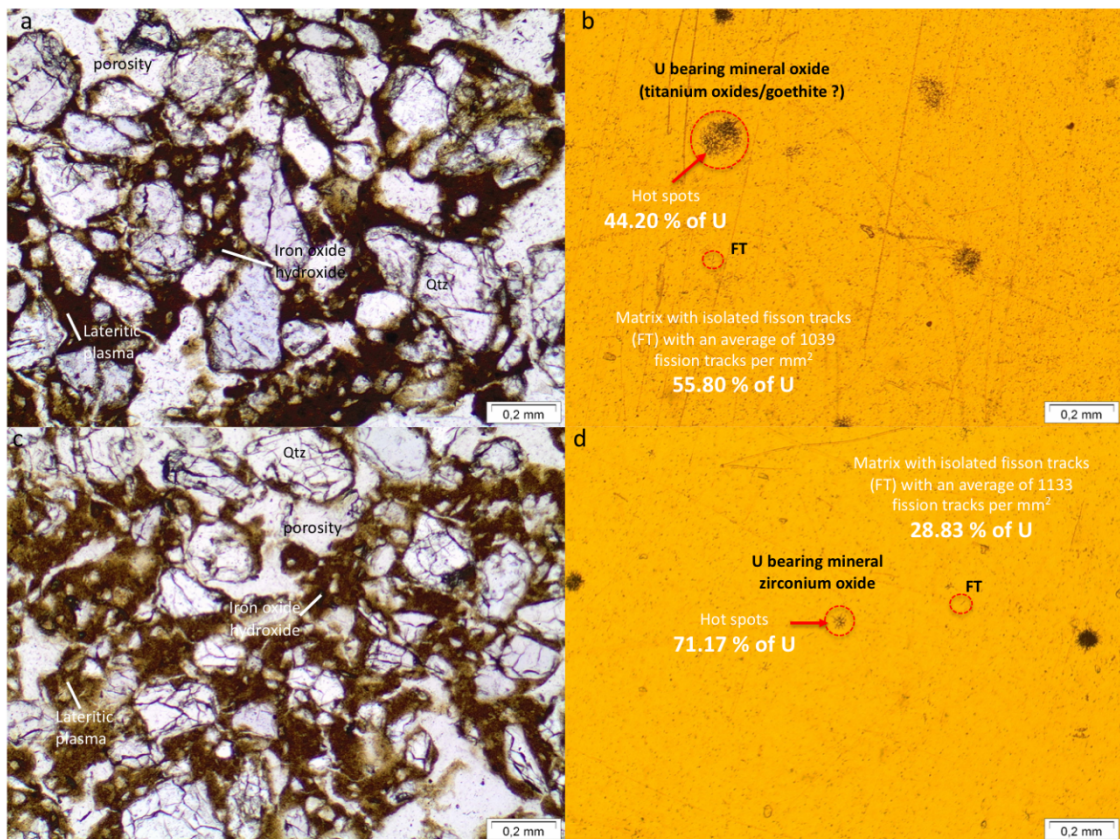
SI 7: Dosimetry curves fitting parameters for artificially irradiated samples from CA and Co2
With m1 the RID's concentration at saturation, m2 the efficiency factor, m3 the natural
paleodose and m4 the linear parameter.

SI 8:

A



B



SI 8: A- General petrographic view of the CA samples, CA 84 (a) and CA 155 (c) and the corresponding fission tracks mapping results (b for CA 84 and d for CA 155). The petrographic organisation of these samples is characterized by a high amount of quartz dispersed with oxides within a lateritic plasma containing kaolinite and iron oxides/hydroxides. **B-** General petrographic view of the CO₂ samples, CO₂ 87 (a) and CO 3875 (c) and the corresponding fission tracks mapping results (b for CO₂ 87 and d for CO 3875). The petrographic organisation of these samples is characterized by a high amount of quartz with a minor content of lateritic plasma and oxides. This is particularly visible for the CO₂ 87 sample.